Supplement of Biogeosciences, 17, 3247–3275, 2020
https://doi.org/10.5194/bg-17-3247-2020-supplement

Biogeosciences Open Access EGU

Supplement of

Assessing the potential for non-turbulent methane escape from the East Siberian Arctic Shelf

Matteo Puglini et al.

Correspondence to: Matteo Puglini (matteo.puglini@mpimet.mpg.de)

S1 From continuity equation to advection-diffusion-reaction equation

Each equation (one per species i) is a specific generalization of a continuity equation with fluxes $\mathscr{F}_i$, related to the the transport processes, and sources/sinks $\mathscr{S}_i$ related to the biogeochemical reactions. It reads:

$$\frac{\partial \xi(z) C_i(z,t)}{\partial t} = -\frac{\partial \mathscr{F}_i(z,t)}{\partial z} + \mathscr{S}_i(z,t). \tag{S1}$$

Where $C_i(z,t)$ is the concentration of the species i (referred to porewater volume if it is a dissolved species or solid matrix volume if it is a solid species) and $\xi(z)$ is the term accounting for this, *i.e.* the porosity $\xi = \varphi$ in case of a dissolved species or the solid fraction $\xi = \varphi_s = 1 - \varphi$ in case of a solid species. The fluxes $\mathscr{F}_i(z,t)$ consist of several components:

- $\mathscr{F}_{D,i}(z,t)$: the molecular diffusive flux (only for dissolved species) is given by the Fick's law

$$\mathscr{F}_{D,i}(z,t) = -D_i(z,t)\varphi(z)\frac{\partial C_i(z,t)}{\partial z} \tag{S2}$$

  where $D_i(z,t)$ is the effective diffusion coefficient. D_i is usually modelled as a time-independent variable and considered constant for each species at a given salinity and temperature and locally only affected by sediment tortuosity $\theta(z)$. The relation between diffusion coefficient and salinity and temperature is provided in Table S6. Tortuosity has been considered strictly linked to porosity $\varphi(z)$ according to $\theta(z) = 1 - \ln \varphi^2(z)$. And porosity follows an exponential decay with depth (Athy, 1930):

$$\varphi(z) = \varphi_0 e^{-c_0 z} \tag{S3}$$

  with φ_0 porosity at the Sediment-Water Interface (SWI) and c_0 typical length scale for compaction (Table S6).

- $\mathscr{F}_{D_b,i}(z,t)$: the bioturbation flux, described as a diffusive flux (to be considered also for solid species), reads

$$\mathscr{F}_{D_b,i}(z,t) = -D_{b,i}(z,t)\xi(z)\frac{\partial C_i(z,t)}{\partial z} \tag{S4}$$

  with $D_b(z,t)$ bioturbation coefficient. Considering no time dependency, the latter is assumed to follow an exponential trend below 5 cm depth, *i.e.* :

$$\begin{cases} D_b(z) = D_b^0, & 0 <= z <= 5 \text{ cm} \\ D_b(z) = D_b^0\, e^{-(z-5)}, & 5 < z < 300 \text{ cm} \end{cases} \tag{S5}$$

  and D_b^0 given in Table S6.

- $\mathscr{F}_{v,i}(z,t)$: the advective flux is given by

$$\mathscr{F}_{v,i}(z,t) = v(z,t)\xi(z)C_i(z,t) \tag{S6}$$

  where $v(z,t)$ is the sedimentation rate $v(z,t) = \omega(z,t)$ for solid species and the sum of sedimentation rate and possible advective flow velocity $v_{up}(z,t)$ for dissolved species, *i.e.* $v(z,t) = \omega(z,t) + v_{up}(z,t)$. If we assume steady state compaction then burial velocity reads (Berner (1980)):

$$\omega(z) = \left(\frac{1-\varphi_0}{1-\varphi(z)}\right)\omega_0 \tag{S7}$$

  with ω_0 sedimentation rate at the SWI. A site where $v_{up} \neq 0$ is denominated as *active* while a site with null upward water velocity is defined as *passive*.

– $\mathscr{F}_{NL,i}(z,t)$ represent any form of non-local transport. In its more classical form (Boudreau (1997)) it is given by bioirrigation provided by irrigated furrows digged by benthic fauna and it reads

$$\mathscr{F}_{irr}(z,t) = -\int_0^z \alpha_i(y)\xi(y)[C_i(0,t) - C_i(y,t)]dy \tag{S8}$$

where $\alpha_i(z)$ is the bioirrigation coefficient, $C_i(0,t)$ is the concentration of the species i at the SWI. Bioirrigation parameter α is modelled as (Thullner et al. (2009)):

$$\alpha(z) = \alpha_0\, e^{-z/z_{irr}} \tag{S9}$$

where α_0 is the bioirrigation coefficient and z_{irr} the bioirrigation attenuation depth (see Table S6). Yet other forms of non-local transport may be considered in the Arctic shelf scenario, such as ice scouring or bubble migration in sediments rich of free gas. These processes are even more difficult to be modelled and are not included in current BRNS version.

With the fluxes described above eq. S1 takes the form of the standard advection-diffusion-reaction equation (see eq. 4) usually implemented in reactive-transport diagenetic models (Berner (1980); Boudreau (1997))

$$\frac{\partial \xi C_i}{\partial t} = \frac{\partial}{\partial z}\left[(D_i + D_{b,i})\xi \frac{\partial C_i}{\partial z}\right] - \frac{\partial}{\partial z}(v\xi C_i) + \alpha_i \xi (C_i(0) - C_i) + \mathscr{S}_i. \tag{S10}$$

S2 Primary redox reactions

Organic matter (OM) decomposition is a complex multi-step process (Arndt et al. (2013)) carried out by micro-organism along a chain of enzyme-mediated biochemical redox reactions which exploits electronic cascades to provide energy. Carbon in organic matter plays the role of electron donor, getting oxidized, and energy yield of the full redox reaction ultimately depends on the terminal electron acceptor (TEA) which overall acts as an oxidant, getting reduced. This entails a preferential sequence of how OM gets mineralized by microorganism along different metabolic pathways with different TEAs according to energy gain ladder.

It determines the typical vertical zonation of the TEAs and byproducts of organic matter decomposition throughout the sediment column according to the redox sequence (Claypool and Kaplan (1974); Froelich et al. (1979); Stumm and Morgan (1996)). The chained reactions involving OM mineralization are reported in Table S2. OM degradation is modeled by a generalized first order kinetic equation, namely decomposition rate is faster the more OM is present. The proportionality between organic carbon decay rate and organic carbon content is set by a degradability rate k which not necessarily has to be constant. We employed reactive continuum model (RCM) to model this degradability rate k as a continuous variable, whose distribution reads:

$$g(k) = \frac{g_0 k^{\nu-1} e^{-ak}}{\Gamma(\nu)} \tag{S11}$$

where g_0 is a scale parameter, ν and a determine the shape of the distribution of k and $\Gamma(\nu)$ is the Gamma function. The quantity a represents the average lifetime of the more reactive organic matter components in a reactive-continuum model (Boudreau and Ruddick (1991)) and the mean degradation constant $\bar{k}$ of the OM spectrum is given by $\bar{k} = \nu/a$. The choice of RCM relies on the fact that it is considered more suitable for marine sediments than a discrete model (Aller and Blair (2004); Arndt et al. (2013)). It manages to encompass all the information about OM degradability in only two parameters, carriers of a theoretical meanings, instead that in as many degradation constants as carbon pools considered in a discrete model. Moreover RCM is more flexible to account for the whole range of degradability that Arctic OM shows, shifting its peak just by tweaking the parameters instead of the initial carbon content of each pool. Another peculiarity of this formulation of RCM is that,

assuming distribution in eq. (S11), OM degradation can actually be rewritten as a first-order kinetic with the a degradability $K(t)$ dependent on sediment age t (Boudreau and Ruddick (1991)), *i.e.*

$$\mathscr{S}_{POC} = \frac{dPOC(t)}{dt} = -K(t)POC(t) = -\frac{\nu}{a+t}POC(t) \tag{S12}$$

where $POC(t)$ is the particulate organic carbon, which in turns reads

$$POC(t) = POC(0)\left(\frac{a}{a+t}\right)^{\nu} \tag{S13}$$

$POC(0)$ being the initial organic carbon concentration. This features allows to estimate sediment age and POC vertical profile just coupling RCM and a discrete model

S3 Estimate of sediment age t and POC content

POC age and vertical profile are critical quantity to be evaluated. One approach would be performing *ab initio* simulations, but they are difficult since a complete knowledge of past boundary conditions and how they evolved over time would be needed. Even when this knowledge is enough, simulation times are usually rather long and hence a different approach is generally used. Using eq. (S7 and S3), in an unperturbed sediment setting, we find that the age at a certain depth z is provided by

$$t(z) = \int_0^z \frac{1}{\omega(z)} = \frac{z + \frac{\varphi_0}{c_0}\left(e^{-c_0 z} - 1\right)}{\omega_0\left(1-\varphi_0\right)}. \tag{S14}$$

If another formulation for the porosity is employed, for instance:

$$\varphi(z) = \varphi_\infty + (\varphi_0 - \varphi_\infty)e^{-c_0 z} \tag{S15}$$

where φ_∞ specifies the asymptotic value of the porosity, then the expression for the age $t(z)$ modifies as:

$$t(z) = \int_0^z \frac{1}{\omega(z)} = \frac{(1-\varphi_\infty)z + \frac{\varphi_0 - \varphi_\infty}{c_0}\left(e^{-c_0 z} - 1\right)}{\omega_0\left(1-\varphi_0\right)}. \tag{S16}$$

If the sediment column were not bioturbated, plugging results (S14) into eq. (S13) would give the steady state profile of the organic matter throughout the whole sediments, with $POC(0)$ POC concentration at the SWI (because considerations above legitimize a *space for time* substitution and initial time corresponds to the uppermost concentration).

The column is instead divided in bioturbated (the upper part) and not-bioturbated (below a certain depth). Because of bioturbation the upper layers are mixed, *i.e.* POC of different ages coexist at the same depth (Meile and Van Cappellen (2005)). This is actually the most difficult problem to be tackled to assign age to a certain sediment level. In order to deal with issue, similarly to (Dale et al., 2015), the POC in the bioturbated zone was modelled resorting to multi-G approximation of the RCM. It means that, within the bioturbated region, the POC is represented by 500 distinct OM fractions, whose reactivity covers the spectrum $k = [k_{min} : 10^{-15}, k_{max} : -log(a) + 2]$ yr^{-1} plus two extra fractions accounting for the reactivity $[0, k_{min}]$ and $[k_{max}, \infty]$. With these considerations and considering constant porosity and sedimentation rate Eq. (S10) reads:

$$\varphi_s \frac{\partial POC(z,t)}{\partial t} = D_b \varphi_s \frac{\partial^2 POC(z,t)}{\partial z^2} - \omega \varphi_s \frac{\partial POC(z,t)}{\partial z} - \varphi_s k_i POC(z,t) \tag{S17}$$

where $\varphi_s = 1 - \varphi$ and k_i is the reactivity of the i-th fraction of POC considered. Eq. (S17) is an advective-diffusive-reactive equation which in steady state can be analytically solved for each fraction i, once boundary conditions are provided. The

general solution is:

$$POC(z) = Ae^{\lambda_1 z} + Be^{\lambda_2 z} \quad \text{where} \quad \begin{cases} \lambda_1 = \dfrac{\omega - \sqrt{\omega^2 + 4D_b k_i}}{2D_b} \\ \lambda_2 = \dfrac{\omega + \sqrt{\omega^2 + 4D_b k_i}}{2D_b}. \end{cases} \tag{S18}$$

In this case boundary conditions are given by

$$\begin{cases} POC(0) = POC_0 \cdot F_i & \text{at } z = 0 \\ D_b \frac{\partial POC}{\partial z} = 0 & \text{at } z = z_{bio} \end{cases} \tag{S19}$$

where F_i is the fraction of initial POC_0 whose reactivity lies around k_i and z_{bio} is the depth of bioturbated zone where we impose that bioturbated flux shall be null. Bearing in mind eq. (S12) and (S13), the distribution of the POC_0 lying around a certain value of $k = k_i$ can be written as:

$$f(k_i) = \frac{g(k_i)}{POC_0} = \frac{a^\nu k_i^{\nu-1} e^{-ak_i}}{\Gamma(\nu)}. \tag{S20}$$

The initial fraction of POC_0 whose reactivity is within $[0, k_i]$, *i.e.* $F(k_i)$, can be obtained via integration of eq. (S20) and this allows to find finally the fraction F_i of POC_0 whose reactivity is in $[k_{i-1}, k_i]$ as

$$F_i = F(k_i) - F(k_{i-1}). \tag{S21}$$

Enforcing boundary conditions (S19) for each of 502 fractions and summing up their solutions we find an approximate solution of the RCM in the bioturbated layer. A comparison between the solution obtained in this way and what should be the RCM solution (eq. (S13)) allows to find the apparent age $t(z)$ of the sediments at each depth within the bioturbated zone and also at its bottom, *i.e.* $t(z_{bio})$. Below the bioturbated zone the apparent age is then found simply adding $t(z_{bio})$ and results of eq. (S14).

The age profile and the POC profile found in this way is then calculated from BRNS at the very beginning and imposed throughout the whole steady-state simulation.

S4 Biogeochemical network: tables

Table S1. The 6 inhibition factors ruling the onset of metabolic pathways according to the succession of the redox ladder.

$$
\begin{array}{ll}
\mathrm{f}_{\mathrm{O_2}} & \begin{cases} 1 & \text{if } [\mathrm{O_2}] > K_{\mathrm{O_2}} \\ \frac{[\mathrm{O_2}]}{K_{\mathrm{O_2}}} & \text{if } [\mathrm{O_2}] < K_{\mathrm{O_2}} \end{cases} \\
\mathrm{f}_{\mathrm{NO_3^-}} & \begin{cases} 0 & \text{if } [\mathrm{O_2}] > K_{\mathrm{O_2}} \\ \left(1 - \frac{[\mathrm{O_2}]}{K_{\mathrm{O_2}}}\right) \frac{\mathrm{NO_3^-}}{K_{\mathrm{NO_3^-}}} & \text{if } [\mathrm{O_2}] < K_{\mathrm{O_2}} \end{cases} \\
\mathrm{f}_{\mathrm{MnO_2}} & \begin{cases} 0 & \text{if } [\mathrm{NO_3^-}] > K_{\mathrm{NO_3^-}} \\ \left(1 - \frac{[\mathrm{O_2}]}{K_{\mathrm{O_2}}} - \frac{[\mathrm{NO_3^-}]}{K_{\mathrm{NO_3^-}}}\right) \frac{\mathrm{MnO_2}}{K_{\mathrm{MnO_2}}} & \text{if } [\mathrm{NO_3^-}] < K_{\mathrm{NO_3^-}} \end{cases} \\
\mathrm{f}_{\mathrm{Fe(OH)_3}} & \begin{cases} 0 & \text{if } [\mathrm{MnO_2}] > K_{\mathrm{MnO_2}} \\ \left(1 - \frac{[\mathrm{O_2}]}{K_{\mathrm{O_2}}} - \frac{[\mathrm{NO_3^-}]}{K_{\mathrm{NO_3^-}}} - \frac{[\mathrm{MnO_2}]}{K_{\mathrm{MnO_2}}}\right) \frac{\mathrm{Fe(OH)_3}}{K_{\mathrm{Fe(OH)_3}}} & \text{if } [\mathrm{MnO_2}] < K_{\mathrm{MnO_2}} \end{cases} \\
\mathrm{f}_{\mathrm{SO_4^{2-}}} & \begin{cases} 0 & \text{if } [\mathrm{Fe(OH)_3}] > K_{\mathrm{Fe(OH)_3}} \\ \left(1 - \frac{[\mathrm{O_2}]}{K_{\mathrm{O_2}}} - \frac{[\mathrm{NO_3^-}]}{K_{\mathrm{NO_3^-}}} - \frac{[\mathrm{MnO_2}]}{K_{\mathrm{MnO_2}}} - \frac{[\mathrm{Fe(OH)_3}]}{K_{\mathrm{Fe(OH)_3}}}\right) \frac{\mathrm{SO_4^{2-}}}{K_{\mathrm{SO_4^{2-}}}} & \text{if } [\mathrm{Fe(OH)_3}] < K_{\mathrm{Fe(OH)_3}} \end{cases} \\
\mathrm{f}_{\mathrm{CH_4}} & \begin{cases} 0 & \text{if } [\mathrm{SO_4^{2-}}] > K_{\mathrm{SO_4^{2-}}} \\ \left(1 - \frac{[\mathrm{O_2}]}{K_{\mathrm{O_2}}} - \frac{[\mathrm{NO_3^-}]}{K_{\mathrm{NO_3^-}}} - \frac{[\mathrm{MnO_2}]}{K_{\mathrm{MnO_2}}} - \frac{[\mathrm{Fe(OH)_3}]}{K_{\mathrm{Fe(OH)_3}}} - \frac{[\mathrm{SO_4^{2-}}]}{K_{\mathrm{SO_4^{2-}}}}\right) \frac{\mathrm{CH_4}}{K_{\mathrm{CH_4}}} & \text{if } [\mathrm{SO_4^{2-}}] < K_{\mathrm{SO_4^{2-}}} \end{cases}
\end{array}
$$

Table S2. The 6 primary redox reactions involved in the degradation of OM. The coefficients x, y and z, enforce Redfield ratio ($x = 106$, $y = 16$ and $z = 1$). SD stands for the conversion factor between solid and liquid volume, *i.e.* $SD = \varphi_s/\varphi$. For the expression of the inhibition factors f see Table S1. $[CH_2O]$ is a shortcut for $(CH_2O)(NH_3)_{\frac{y}{x}}(H_3PO_4)_{\frac{z}{x}}$, to take into account nutrients.

#	Reaction	Rate expression
R1	$[CH_2O] + \left(\frac{x+2y}{x}\right) SD \cdot O_2 + \left(\frac{y+2z}{x}\right) SD \cdot {HCO_3}^- \longrightarrow \left(\frac{x+y+2z}{x}\right) SD \cdot CO_2 + \left(\frac{y}{x}\right) SD \cdot {NO_3}^- + \left(\frac{z}{x}\right) SD \cdot {HPO_4}^{2-} + \left(\frac{x+2y+2z}{x}\right) SD \cdot H_2O$	$\frac{\nu}{a+t}[CH_2O] \cdot f_{O_2}$
R2	$[CH_2O] + \left(\frac{4x+3y}{5x}\right) SD \cdot {NO_3}^- \longrightarrow \left(\frac{x-3y+10z}{5x}\right) SD \cdot CO_2 + \left(\frac{4x+3y-10z}{5x}\right) SD \cdot {HCO_3}^- + \left(\frac{z}{x}\right) SD \cdot {HPO_4}^{2-} + \left(\frac{3x+6y+10z}{5x}\right) H_2O + \left(\frac{2x+4y}{5x}\right) N_2$	$\frac{\nu}{a+t}[CH_2O] \cdot f_{{NO_3}^-}$
R3	$[CH_2O] + 2MnO_2 + \left(\frac{3x+y-2z}{x}\right) SD \cdot CO_2 + \left(\frac{x+y-2z}{x}\right) SD \cdot H_2O \longrightarrow 2SD \cdot {Mn}^{2+} + \left(\frac{y}{x}\right) SD \cdot {NH_4}^+ + \left(\frac{4x+y-2z}{x}\right) SD \cdot {HCO_3}^- + \left(\frac{z}{x}\right) SD \cdot {HPO_4}^{2-}$	$\frac{\nu}{a+t} \cdot [CH_2O] \cdot f_{MnO_2}$
R4	$[CH_2O] + 4Fe(OH)_3 + \left(\frac{7x+y-2z}{x}\right) SD \cdot CO_2 \longrightarrow 4SD \cdot {Fe}^{2+} + \left(\frac{8x+y-2z}{x}\right) SD \cdot {HCO_3}^- + \left(\frac{y}{x}\right) SD \cdot {NH_4}^+ + \left(\frac{z}{x}\right) SD \cdot {HPO_4}^{2-} + \left(\frac{3x-y+2z}{x}\right) H_2O$	$\frac{\nu}{a+t} \cdot [CH_2O] \cdot f_{Fe(OH)_3}$
R5	$[CH_2O] + \frac{1}{2}SD \cdot {SO_4}^{2-} + \left(\frac{y-2z}{x}\right) SD \cdot CO_2 + \left(\frac{y-2z}{x}\right) SD \cdot H_2O \longrightarrow \left(\frac{x+y-2z}{x}\right) SD \cdot {HCO_3}^- + \left(\frac{y}{x}\right) SD \cdot {NH_4}^+ + \frac{1}{2}SD \cdot H_2S + \left(\frac{z}{x}\right) SD \cdot {HPO_4}^{2-}$	$\frac{\nu}{a+t} \cdot [CH_2O] \cdot f_{{SO_4}^{2-}}$
R6	$[CH_2O] \longrightarrow \left(\frac{x-2y+4z}{2x}\right) SD \cdot CO_2 + \left(\frac{y-2z}{x}\right) SD \cdot {HCO_3}^- + \left(\frac{y}{x}\right) SD \cdot {NH_4}^+ + \frac{1}{2}SD \cdot CH4 + \left(\frac{z}{x}\right) SD \cdot {HPO_4}^{2-}$	$\frac{\nu}{a+t} \cdot [CH_2O] \cdot f_{CH_4}$

Table S3. The secondary redox, precipitation, absorption and equilibrium reactions

#	Reaction	Rate expression
R7	$2\,O_2 + NH_4{}^+ + 2\,HCO_3{}^- \longrightarrow NO_3{}^- + 2\,CO_2 + 3\,H_2O$	$k_7[O_2][NH_4{}^+]$
R8	$\frac{1}{2}O_2 + Mn^{2+} + 2\,HCO_3{}^- \longrightarrow \frac{MnO_2}{SD} + 2\,CO_2 + H_2O$	$k_8[O_2][Mn^{2+}]$
R9	$MnO_2 + 2SD \cdot Fe^{2+} + 2SD \cdot HCO_3{}^- + 2SD \cdot H_2O \longrightarrow$ $2\,Fe(OH)_3 + SD \cdot Mn^{2+} + 2SD \cdot CO_2$	$k_9[Fe^{2+}][MnO_2]$
R10	$\frac{1}{4}O_2 + Fe^{2+} + 2\,HCO_3{}^- + \frac{1}{2}\,H_2O \longrightarrow \frac{Fe(OH)_3}{SD} + 2\,CO_2$	$k_{10}[O_2][Fe^{2+}]$
R11	$2\,O_2 + H_2S + 2\,HCO_3{}^- \longrightarrow SO_4{}^{2-} + 2\,CO_2 2\,H_2O$	$k_{11}[O_2]\left([H_2S] + [HS^-]\right)$
R12	$MnO_2 + SD \cdot H_2S + 2SD \cdot CO_2 \longrightarrow$ $S^0 + SD \cdot Mn^{2+} + 2SD \cdot HCO_3{}^-$	$k_{12}[MnO_2]\left([H_2S] + [HS^-]\right)$
R13	$2Fe(OH)_3 + SD \cdot H_2S + 4SD \cdot CO_2 \longrightarrow$ $S^0 + 2SD \cdot Fe^{2+} + 4SD \cdot HCO_3{}^-$	$k_{13}[Fe(OH)_3]\left([H_2S] + [HS^-]\right)$
R14	$CH_4 + 2\,O_2 \longrightarrow CO_2 + 2\,H_2O$	$k_{14}[CH_4][O_2]$
R15	$FeS + SD \cdot O_2 \longrightarrow S^0 + SD \cdot Fe^{2+} + SD \cdot SO_4{}^{2-}$	$k_{15}[FeS][O_2]$
R16	$Mn^{2+} + 2HCO_3{}^- \longrightarrow \frac{MnCO3}{SD} + CO_2 + H_2O$	$\begin{cases} k_{16}\left(\frac{[Mn^{2+}][CO_3{}^{2-}]}{K_{s\,MnCO_3}} - 1\right) & \text{if } [Mn^{2+}][CO_3{}^{2-}] > K_{s\,MnCO_3} \\ 0 & \text{if } [Mn^{2+}][CO_3{}^{2-}] < K_{s\,MnCO_3} \end{cases}$
R17	$Fe^{2+} + H_2S + 2HCO_3{}^- \longrightarrow \frac{FeS}{SD} + 2CO_2 + 2H_2O$	$\begin{cases} k_{17}\left(\frac{[Fe^{2+}][HS^-]}{[H^+]K_{s\,FeS}} - 1\right) & \text{if } \frac{[Fe^{2+}][HS^-]}{[H^+]} > K_{s\,FeS} \\ 0 & \text{if } \frac{[Fe^{2+}][HS^-]}{[H^+]} < K_{s\,FeS} \end{cases}$
R18	$\frac{FeS}{SD} + 2\,CO_2 + 2H_2O \longrightarrow Fe^{2+} + H_2S + 2HCO_3{}^-$	$\begin{cases} k_{18}\left(1 - \frac{[Fe^{2+}][HS^-]}{[H^+]K_{s\,FeS}}\right) & \text{if } \frac{[Fe^{2+}][H_2S]}{[H^+]} < K_{s\,FeS} \\ 0 & \text{if } \frac{[Fe^{2+}][H_2S]}{[H^+]} > K_{s\,FeS} \end{cases}$
R19	$Fe^{2+} + 2HCO_3{}^- \longrightarrow FeCO_3 + CO_2 + H_2O$	$\begin{cases} k_{19}\left(\frac{[Fe^{2+}][CO_3{}^{2-}]}{K_{s\,FeCO_3}} - 1\right) & \text{if } [Fe^{2+}][CO_3{}^{2-}] > K_{s\,FeCO_3} \\ 0 & \text{if } [Fe^{2+}][CO_3{}^{2-}] < K_{s\,FeCO_3} \end{cases}$

R20	$\mathrm{FeS} + \mathrm{SD} \cdot \mathrm{H_2S} \longrightarrow \mathrm{FeS_2}$	$k_{20}[\mathrm{FeS}]\left([\mathrm{H_2S}] + [\mathrm{HS^-}]\right)$
R21	$3\,\mathrm{FeS} + \mathrm{SD} \cdot \mathrm{S^0} \longrightarrow \mathrm{Fe_3S_4}$	$k_{21}[\mathrm{FeS}][\mathrm{S^0}]$
R22	$\mathrm{{PO_4}^{3-}} \longrightarrow CFA$	$\begin{cases} k_{22}\left([\mathrm{{PO_4}^{3-}}] - [\mathrm{{PO_4}^{3-}}]^*\right) & \text{if } [\mathrm{{PO_4}^{3-}}] > [\mathrm{{PO_4}^{3-}}]^* \\ 0 & \text{if } [\mathrm{{PO_4}^{3-}}] < [\mathrm{{PO_4}^{3-}}]^* \end{cases}$
R23	$\mathrm{CaCO_3} + \mathrm{SD} \cdot \mathrm{H^+} \longrightarrow \mathrm{SD} \cdot \mathrm{Ca^{2+}} + \mathrm{SD} \cdot \mathrm{HCO_3^-}$	$\begin{cases} k_{23}\left(1 - \frac{[\mathrm{Ca^{2+}}][\mathrm{{CO_3}^{2-}}]}{K_{s\mathrm{CaCO_3}}}\right) & \text{if } [\mathrm{Ca^{2+}}][\mathrm{{CO_3}^{2-}}] < K_{s\mathrm{CaCO_3}} \\ 0 & \text{if } [\mathrm{Ca^{2+}}][\mathrm{{CO_3}^{2-}}] > K_{s\mathrm{CaCO_3}} \end{cases}$
R24	$\mathrm{Ca^{2+}} + \mathrm{HCO_3^-} \longrightarrow \frac{CaCO3}{SD} + \mathrm{H^+}$	$\begin{cases} k_{24}\left(\frac{[\mathrm{Ca^{2+}}][\mathrm{{CO_3}^{2-}}]}{K_{s\mathrm{CaCO_3}}} - 4.5\right) & \text{if } \frac{[\mathrm{Ca^{2+}}][\mathrm{{CO_3}^{2-}}]}{K_{s\mathrm{CaCO_3}}} > 4.5 \\ 0 & \text{if } \frac{[\mathrm{Ca^{2+}}][\mathrm{{CO_3}^{2-}}]}{K_{s\mathrm{CaCO_3}}} < 4.5 \end{cases}$
R25	$\mathrm{CH_4(g)} \longrightarrow \mathrm{CH_4(aq)}$	$\begin{cases} k_{25}[\mathrm{CH_4(g)}]\left([\mathrm{CH_4}]^* - [\mathrm{CH_4}]\right) & \text{if } [\mathrm{CH_4}] < [\mathrm{CH_4}]^* \\ 0 & \text{if } [\mathrm{CH_4}] > [\mathrm{CH_4}]^* \end{cases}$
R26	$\mathrm{CH_4(aq)} \longrightarrow \mathrm{CH_4(g)}$	$\begin{cases} k_{26}\left([\mathrm{CH_4}] - [\mathrm{CH_4}]^*\right) & \text{if } [\mathrm{CH_4}] > [\mathrm{CH_4}]^* \\ 0 & \text{if } [\mathrm{CH_4}] < [\mathrm{CH_4}]^* \end{cases}$
R27	$4\,\mathrm{S^0} + 4\,\mathrm{H_2O} \longrightarrow \mathrm{{SO_4}^{2-}} + 3\mathrm{H_2S} + 2\mathrm{H^+}$	$k_{27}[\mathrm{S^0}]$
R28	$\mathrm{{NH_4}^+(aq)} \longrightarrow \mathrm{{NH_4}^+(ads)}$	$k_{28}^f[\mathrm{{NH_4}^+}(aq)]\varphi - k_{28}^b[\mathrm{{NH_4}^+(ads)}]\varphi_s$
R29	$\mathrm{{PO_4}^{3-}(aq)} \longrightarrow \mathrm{{PO_4}^{3-}(ads)}$	$k_{29}^f[\mathrm{{PO_4}^{3-}}(aq)]\varphi - k_{29}^b[\mathrm{{PO_4}^{3-}(ads)}]\varphi_s$
R30	$\mathrm{Fe^{2+}(aq)} \longrightarrow \mathrm{Fe^{2+}(ads)}$	$k_{30}^f[\mathrm{Fe^{2+}(aq)}]\varphi - k_{30}^b[\mathrm{Fe^{2+}(ads)}]\varphi_s$
R31	$\mathrm{FeOH_3} + \mathrm{{PO_4}^{-3}} \longrightarrow \mathrm{PO_4(ads_{Fe(OH)3})}$	$k_{31}^f[\mathrm{{PO_4}^{3-}}][\mathrm{Fe(OH)_3}] - k_{31}^b[\mathrm{PO_4(ads_{Fe(OH)3})}]$
R32	$\mathrm{CO_2} + \mathrm{H_2O} \longrightarrow \mathrm{H^+} + \mathrm{HCO_3^-}$	k_{32} thermodynamic equilibrium
R33	$\mathrm{HCO_3^-} \longrightarrow \mathrm{H^+} + \mathrm{{CO_3}^{2-}}$	k_{33} thermodynamic equilibrium
R34	$\mathrm{H_2S} \longrightarrow \mathrm{H^+} + \mathrm{HS^-}$	k_{34} thermodynamic equilibrium
R35	$\mathrm{B(OH)_3} \longrightarrow \mathrm{{B(OH)_4}^-} + \mathrm{H^+}$	k_{35} thermodynamic equilibrium

S5 Model validations

S5.1 Sediment core offshore the Laptev Sea

Table S4. Model boundary parameters and boundary conditions for the case study of a site offshore the Laptev Sea, Russia (core 14-3). Values with (!) are set for this study. All the other variables are as in Brüchert et al. (2018) and Brüchert (2020). $[\,]_-$ stands for lower boundary conditions (at 3 m depth), while $[\,]_+$ stand for upper boundary conditions. "Extrapolation" means that the value has been extrapolated from data.

Quantity	Value	Units
$a(!)$	10	yr
$\nu(!)$	0.200	-
v_{up}	0.0	cm yr^{-1}
$[{SO_4}^{2-}]_+$	27.95	mM
$[O_2]_+$	326.61	μM
$[CH_4]_+$	0.0	nM
$[CH_4]_-(!)$	16.0	mM
$[CH_4]^*$	14.0	mM
$[{NH_4}^+]_+$	8.0	μM (extrapolation)
$k_{AOM}(!)$	$1.0 \cdot 10^4$	M^{-1} yr^{-1}
$k_{28}^f(!)$	500	yr^{-1}
$[{PO_4}^{3-}]^*(!)$	75.0	μM

Table S5. Organic carbon content (Brüchert, 2020) for a site offshore the Laptev Sea, Russia (core 14-3). The average density of the sediment matrix is 2.76 g cm^{-3} (Brüchert et al., 2018).

Depth [cm]	Organic Carbon content [%]
3	0.88
5	0.29
7	0.51
9	0.84
11	0.59
14.5	0.72
17	0.74
19	0.4

S6 Sensitivity study: model parameters and model boundary conditions. Tables

Table S6. Generic model parameters. The parameters below the red line at the bottom are the quantities involved in the bioenergetic formulation of AOM. Diffusion coefficients depends on temperature $T(^{\circ}C)$, salinity S and porosity φ according to the relation $D(T,S,\varphi) = \frac{D(1+\mu T(^{\circ}C))}{1-\ln\left(\varphi^2\right)}$.

Quantity	Value	Units	Reference
ν	0.125	-	This study
SD	φ_s/φ	-	Athy (1930)
S	20	psu	This study
ρ	2.41	g cm^{-3}	Berg (2003)
D_b^0	29.8	cm^2 yr^{-1}	Middelburg et al. (1997)
z_{bio}	5	cm^2 yr^{-1}	Boudreau (1997)
z_{irr}	3.5	cm	Thullner et al. (2009)
T	0, 273.15	°C, K	This study
C:N	106:16	-	Redfield ratio
C:P	106:1	-	Redfield ratio
D_{O_2}, μ_{O_2}	380.45, 0.06	cm^2 yr^{-1}, T^{-1}	Dale et al. (2012)
$D_{NO_3^-}$, $\mu_{NO_3^-}$	394.59, 0.038	cm^2 yr^{-1}, T^{-1}	Van Cappellen and Wang (1996)
$D_{SO_4^{2-}}$, $\mu_{SO_4^{2-}}$	173.92, 0.045	cm^2 yr^{-1}, T^{-1}	Dale et al. (2012)
D_{CH_4}, μ_{CH_4}	263.94, 0.052	cm^2 yr^{-1}, T^{-1}	Van Cappellen and Wang (1996)
$D_{NH_4^+}$, $\mu_{NH_4^+}$	395.87, 0.041	cm^2 yr^{-1}, T^{-1}	Van Cappellen and Wang (1996)
$D_{PO_4^{3-}}$, $\mu_{PO_4^{3-}}$	112.36, 0.054	cm^2 yr^{-1}, T^{-1}	Van Cappellen and Wang (1996)
$D_{Mn^{2+}}$, $\mu_{Mn^{2+}}$	123.39, 0.05	cm^2 yr^{-1}, T^{-1}	Van Cappellen and Wang (1996)
$D_{Fe^{2+}}$, $\mu_{Fe^{2+}}$	136.24, 0.044	cm^2 yr^{-1}, T^{-1}	Dale et al. (2012)
D_{H_2S}, μ_{H_2S}	331.61, 0.06	cm^2 yr^{-1}, T^{-1}	Van Cappellen and Wang (1996)
D_{HS^-}, μ_{HS^-}	392.02, 0.031	cm^2 yr^{-1}, T^{-1}	Van Cappellen and Wang (1996)
$D_{CH_4(g)}$, $\mu_{CH_4(g)}$	5000.0, 0.0	cm^2 yr^{-1}, T^{-1}	Van Cappellen and Wang (1996)
$D_{H_2CO_3}$, $\mu_{H_2CO_3}$	320.04, 0.06	cm^2 yr^{-1}, T^{-1}	Van Cappellen and Wang (1996)
$D_{HCO_3^-}$, $\mu_{HCO_3^-}$	217.22, 0.048	cm^2 yr^{-1}, T^{-1}	Van Cappellen and Wang (1996)

$D_{{CO_3}^{2-}}$, $\mu_{{CO_3}^{2-}}$	176.09, 0.047	$cm^2\ yr^{-1}$, T^{-1}	Van Cappellen and Wang (1996)
$D_{B(OH)_3}$, $\mu_{B(OH)_3}$	110.05, 0.054	$cm^2\ yr^{-1}$, T^{-1}	Van Cappellen and Wang (1996)
$D_{{B(OH)_4}^-}$, $\mu_{{B(OH)_4}^-}$	96.30, 0.041	$cm^2\ yr^{-1}$, T^{-1}	Van Cappellen and Wang (1996)
D_{H^+}, μ_{H^+}	600.0, 0.05	$cm^2\ yr^{-1}$, T^{-1}	Van Cappellen and Wang (1996)
$D_{Ca^{2+}}$, $\mu_{Ca^{2+}}$	150.38, 0.045	$cm^2\ yr^{-1}$, T^{-1}	Van Cappellen and Wang (1996)
D_{S^0}, μ_{S^0}	173.92, 0.045	$cm^2\ yr^{-1}$, T^{-1}	Van Cappellen and Wang (1996)
φ_0	0.45	-	LaRowe et al. (2017)
c_0	$0.5 \cdot 10^{-3}$	m^{-1}	LaRowe et al. (2017)
φ_∞	0.35	-	This study
K_{O_2}	8	μM	Thullner et al. (2009)
$K_{{NO_3}^-}$	5	μM	Van Cappellen and Wang (1996)
K_{MnO_2}	2	$\mu mol/g_d$	Thullner et al. (2009)
$K_{Fe(OH)_3}$	5	$\mu mol/g_d$	Thullner et al. (2009)
$K_{{SO_4}^{2-}}$	100	μM	Dale et al. (2006)
k_7	$1.0 \cdot 10^7$	$cm^3\ mol^{-1}\ yr^{-1}$	Van Cappellen and Wang (1996)
k_8	$2.0 \cdot 10^9$	$M^{-1}\ yr^{-1}$	Thullner et al. (2009)
k_9	$2.0 \cdot 10^8$	$M^{-1}\ yr^{-1}$	Thullner et al. (2009)
k_{10}	$1.0 \cdot 10^{11}$	$cm^3\ mol^{-1}\ yr^{-1}$	Van Cappellen and Wang (1996)
k_{11}	$1.0 \cdot 10^9$	$cm^3\ mol^{-1}\ yr^{-1}$	Van Cappellen and Wang (1996)
k_{12}	$1.0 \cdot 10^4$	$M^{-1}\ yr^{-1}$	Thullner et al. (2009)
k_{13}	$1.0 \cdot 10^4$	$M^{-1}\ yr^{-1}$	Thullner et al. (2009)
k_{14}	$1.0 \cdot 10^{13}$	$cm^3\ mol^{-1}\ yr^{-1}$	Van Cappellen and Wang (1996)
k_{15}	$1.0 \cdot 10^9$	$cm^3\ mol^{-1}\ yr^{-1}$	Van Cappellen and Wang (1996)
k_{16}	$1.0 \cdot 10^{-8}$	$mol\ cm^{-3}\ yr^{-1}$	Van Cappellen and Wang (1996)
k_{17}	$5 \cdot 10^{-9}$	$mol\ cm^{-3}\ yr^{-1}$	Van Cappellen and Wang (1996)
k_{18}	$1.0 \cdot 10^{-3}$	$mol\ cm^{-3}\ yr^{-1}$	Van Cappellen and Wang (1996)
k_{19}	$1.0 \cdot 10^{-9}$	$mol\ cm^{-3}\ yr^{-1}$	Van Cappellen and Wang (1996)
k_{20}	$6.0 \cdot 10^7$	$cm^3\ mol^{-1}\ yr^{-1}$	Van Cappellen and Wang (1996)
k_{21}	$2.4 \cdot 10^4$	$cm^3\ mol^{-1}\ yr^{-1}$	Van Cappellen and Wang (1996)
k_{22}	1	yr^{-1}	Van Cappellen and Wang (1996)
k_{23}	0.1	$mol\ cm^{-3}\ yr^{-1}$	Van Cappellen and Wang (1996)
k_{24}	24.16	$M^{-1}\ yr^{-1}$	Wallmann et al. (2006)
k_{25}	$1.0 \cdot 10^9$	$cm^3\ mol^{-1}\ yr^{-1}$	Van Cappellen and Wang (1996)
k_{26}	$7.89 \cdot 10^2$	yr^{-1}	Pauss et al. (1990)
k_{27}	$1.0 \cdot 10^{-3}$	yr^{-1}	Van Cappellen and Wang (1996)
k_{28}^f	1.6	yr^{-1}	Van Cappellen and Wang (1996)
k_{28}^b	1.0	yr^{-1}	Van Cappellen and Wang (1996)
k_{29}^f	1.8	yr^{-1}	Van Cappellen and Wang (1996)
k_{29}^b	1.0	yr^{-1}	Van Cappellen and Wang (1996)
k_{30}^f	400	yr^{-1}	Van Cappellen and Wang (1996)
k_{30}^b	1.0	yr^{-1}	Van Cappellen and Wang (1996)
k_{31}^f	100	yr^{-1}	Van Cappellen and Wang (1996)
k_{31}^b	1.0	yr^{-1}	Van Cappellen and Wang (1996)
k_{32}	$8.470 \cdot 10^{-7}$	M	Millero (1995)
k_{33}	$4.300 \cdot 10^{-10}$	M	Millero (1995)
k_{34}	$1.602 \cdot 10^{-7}$	M	Millero (1995)
k_{35}	$1.318 \cdot 10^{-9}$	M	Millero (1995)

$[CH_4]^*$	5.46	mM	Dale et al. (2008a)
$[PO_4^{3-}]^*$	10	μM	This study
K_{sMnCO_3}	$3.2 \cdot 10^{-9}$	M^2	Van Cappellen and Wang (1996)
K_{sFeCO_3}	$4.0 \cdot 10^{-9}$	M^2	Van Cappellen and Wang (1996)
K_{sFeS}	$8.2 \cdot 10^{-4}$	M	Van Cappellen and Wang (1996)
K_{sCaCO_3}	$3.8 \cdot 10^{-7}$	M^2	Mucci (1983); Millero (1995)
μ_g	18.3	yr^{-1}	Dale et al. (2006, 2008b)
μ_d	0.1	yr^{-1}	Dale et al. (2006, 2008b)
γ	2.48	-	Dale et al. (2006, 2008b)
χ	8.0	-	Dale et al. (2006, 2008b)
ΔG_{BQ}	20	kJ/mol e^-	Dale et al. (2006, 2008b)
ΔG_r^0	-29.92	kJ/mol e^-	Regnier et al. (2011)
$K_m^{CH_4}$	$1.5 \cdot 10^{-3}$	M	Dale et al. (2006, 2008b)
$K_m^{SO_4^{2-}}$	$1.0 \cdot 10^{-3}$	M	Dale et al. (2006, 2008b)

Table S7. Generic model upper boundary conditions. The boundary condition for biomass is applied only in the bioenergetic formulation of AOM

Species	Value @ SWI	Units	Reference
POC	1.04	%	This study
O_2	306.98	μM	Garcia et al. (2010a)
NO_3^-	11.51	μM	Garcia et al. (2010b)
MnO_2	2.18	μmol cm^{-2} yr^{-1}	Dale et al. (2015); Glasby (2006)
$Fe(OH)_3$	7.09	μmol cm^{-2} yr^{-1}	Dale et al. (2015); Glasby (2006)
SO_4^{2-}	28.0	mM	Thullner et al. (2009)
CH_4	0.0	mM	This study
NH_4^+	0.0	mM	This study
PO_4^{3-}	1.0	μM	Sales de Freitas (2018)
Mn^{2+}	1.0	μM	Sales de Freitas (2018)
Fe^{2+}	1.0	pM	Sales de Freitas (2018)
H_2S	0.835	nM	Sales de Freitas (2018)
HS^-	9.17	nM	Sales de Freitas (2018)
$CH_4(g)$	0.0	nM	This study
H_2CO_3	39	μM	Sales de Freitas (2018)
HCO_3^-	2150	μM	Sales de Freitas (2018)
CO_3^{2-}	15.3	μM	Sales de Freitas (2018)
$B(OH)_3$	363.6	μM	Sales de Freitas (2018)
$B(OH)_4^-$	61.4	μM	Sales de Freitas (2018)
H^+	6.31	μM	Sales de Freitas (2018)
$CaCO_3$	23	μmol cm^{-2} yr^{-1}	Sales de Freitas (2018)
Ca^{2+}	9.7	mM	Sales de Freitas (2018)
$NH_4^+(ads)$	0	mM	Sales de Freitas (2018)
$PO_4^{3-}(ads)$	0	mM	Sales de Freitas (2018)
FeS	0	μmol cm^{-2} yr^{-1}	Sales de Freitas (2018)
$FeCO_3$	0	mM	Sales de Freitas (2018)

S^0	0	mM	Sales de Freitas (2018)
FeS_2	0	μmol cm^{-2} yr^{-1}	Sales de Freitas (2018)
$Fe^{2+}(ads)$	0	mM	Sales de Freitas (2018)
$PO_4(ads_{Fe(OH)3})$	0	Mm	Sales de Freitas (2018)
B	$1.0 \cdot 10^8$, $3.158 \cdot 10^7$	mol cm^{-3}, cells cm^{-3}	This study

Table S8. AOM Damköhler number for $\omega = 0.123$ cm yr^{-1} and $\omega = 1.5$ cm yr^{-1}. The reported values are the average of the maximum and minimum resulting from simulations with different bottom methane concentration. Missing values are because simulations were not run with the corresponding pair of parameters.

		v_{up} [cm yr^{-1}]						
		0	0.3	0.5	1	3	7	10
ω [cm yr^{-1}]	0.123	1206	1124	683	327	120	52	32
		1521	1473	772	409	139	57	42
	1.5	470	-	-	1408	-	-	-
		518			1630			

Table S9. Name, location, water depth and linear sedimentation rate for cores used to inter- and extra-polate the sedimentation rates to the whole Laptev sea area via simple 3D kriging.

Core name	Lon (°)	Lat (°)	Water depth (m)	ω (cm/yr)	Reference
KD9502-14	133.117	76.192	46	0.003	Bauch et al. (2001)
PM9462-4	136.005	74.503	27	0.05	Bauch et al. (2001)
PM9499-2	115.545	75.501	48	0.004	Bauch et al. (2001)
PM9402-3	115.249	75.491	47	0.16	Strobl et al. (1998)
PM9417-4	130.014	75.503	51	0.08	Strobl et al. (1998)
PM9442-3	126.003	74.501	40	0.13	Strobl et al. (1998)
PM9462-1	136.004	74.502	27	0.12	Strobl et al. (1998)
PM9463-8	126.582	74.504	36	0.35	Strobl et al. (1998)
PM9481-2	134.004	73.750	17	0.17	Strobl et al. (1998)
PM9482-1	128.175	73.999	27	0.39	Strobl et al. (1998)
PS51/080-13	131.638	73.459	21	0.028	Bauch et al. (2001)
PS51/092-13	130.136	74.594	32	0.07	Bauch et al. (2001)
PS51/092-12	130.138	74.593	32	0.041	Bauch et al. (2001)
PS51/118-2	132.237	77.892	114	0.002	Bauch et al. (2001)
PS51/118-3	132.199	77.892	122	0.008	Bauch et al. (2001)
PS51/135-4	133.243	76.165	51	0.031	Bauch et al. (2001)
PS51/141-2	128.641	75.227	42	0.011	Bauch et al. (2001)
PS51/154-11	120.610	77.276	270	0.012	Bauch et al. (2001)
PS51/159-10	116.032	76.767	60	0.011	Bauch et al. (2001)
PS2458-4	133.398	78.167	983	0.027	Bauch et al. (2001)
L13-09-2	129.895	73.018	10	0.45	Han (2014)
L13-14-2	130.695	73.857	25	0.16	Han (2014)

L13-18-2	130.479	73.032	16	0.3	Han (2014)
L13-04-2	130.690	71.902	15	0.2	Han (2014)
C-37	130.367	71.617	10	0.024	Stein and Fahl (2000)
C-4	131.000	73.167	26	0.17	Stein and Fahl (2000)
C-7	129.983	74.883	37	0.159	Stein and Fahl (2000)
C-8	130.500	75.400	48	0.015	Stein and Fahl (2000)
C-11	130.083	76.867	66	0.011	Stein and Fahl (2000)
PS2725-5	144.135	78.656	77	0.013	Stein et al. (2001)
PS2778-2	113.065	77.978	341	0.038	Stein et al. (2001)
PS2476-4	118.193	77.39	521	0.05	Stein et al. (2001)
PS2742-5	103.815	80.788	1890	0.022	Stein et al. (2001)
PS2474-3	118.575	77.67	1494	0.02	Stein et al. (2001)
PS2741-1	105.395	81.105	2400	0.012	Stein et al. (2001)
PS2471-4	119.793	79.152	3047	0.002	Stein et al. (2001)

S6.1 Sensitivity study: model parameters and model boundary conditions. Figures

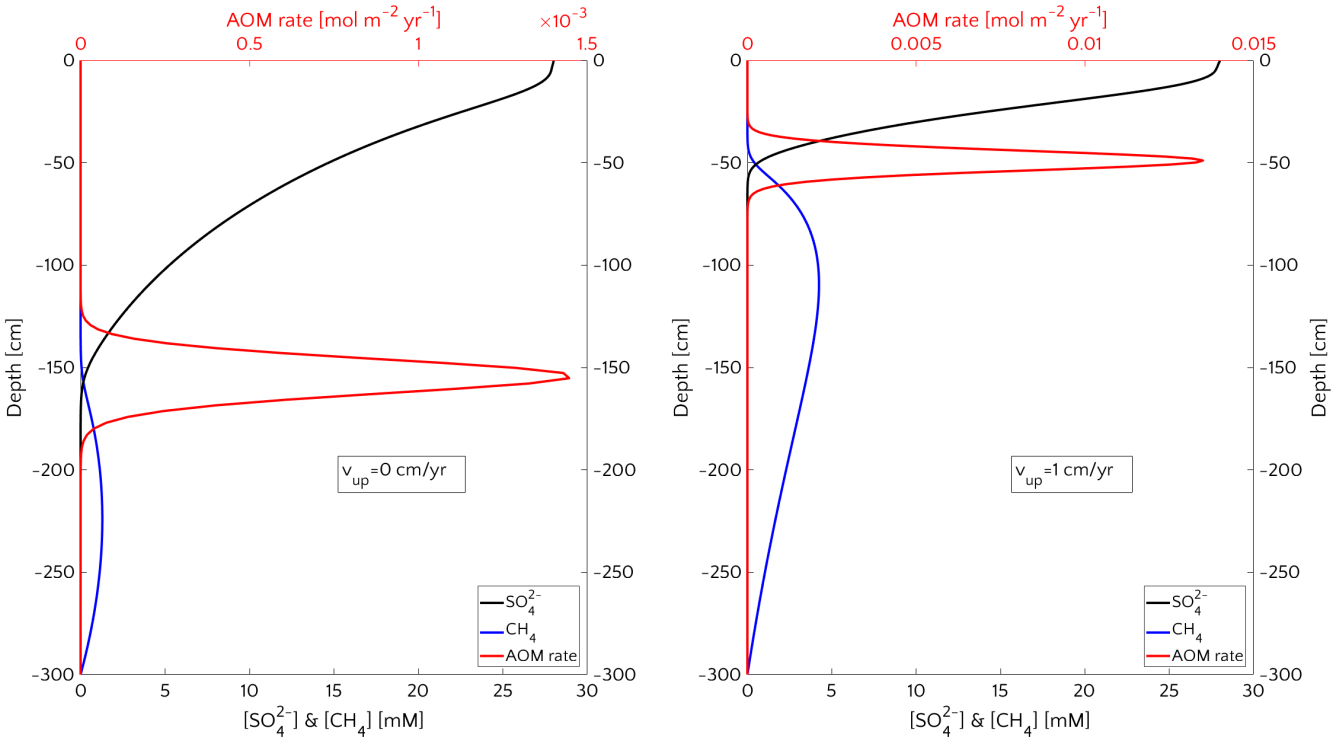

Figure S1. Outcomes for the baseline simulations at steady state. Passive case (left) and active case with $v_{up} = 1$ cm/yr (right). Typical SMTZ shoaling (from 155.2 cm to 48.9 cm) and squeezing (from 65 cm to 38 cm) from passive to active case.

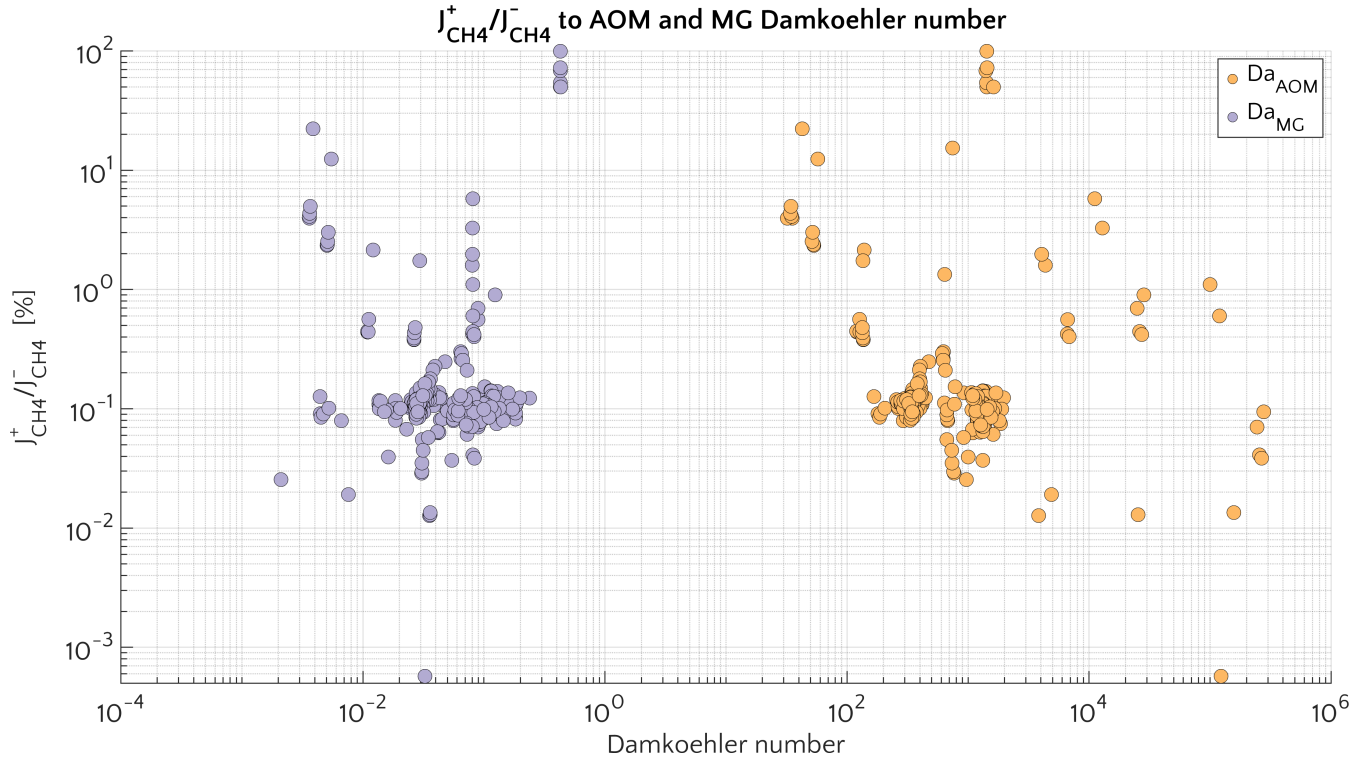

Figure S2. Ratio J^{+}_{CH4}/J^{-}_{CH4} (in %) as a function pf the Damköler numbers for AOM (orange) and for methanogenesis (purple)

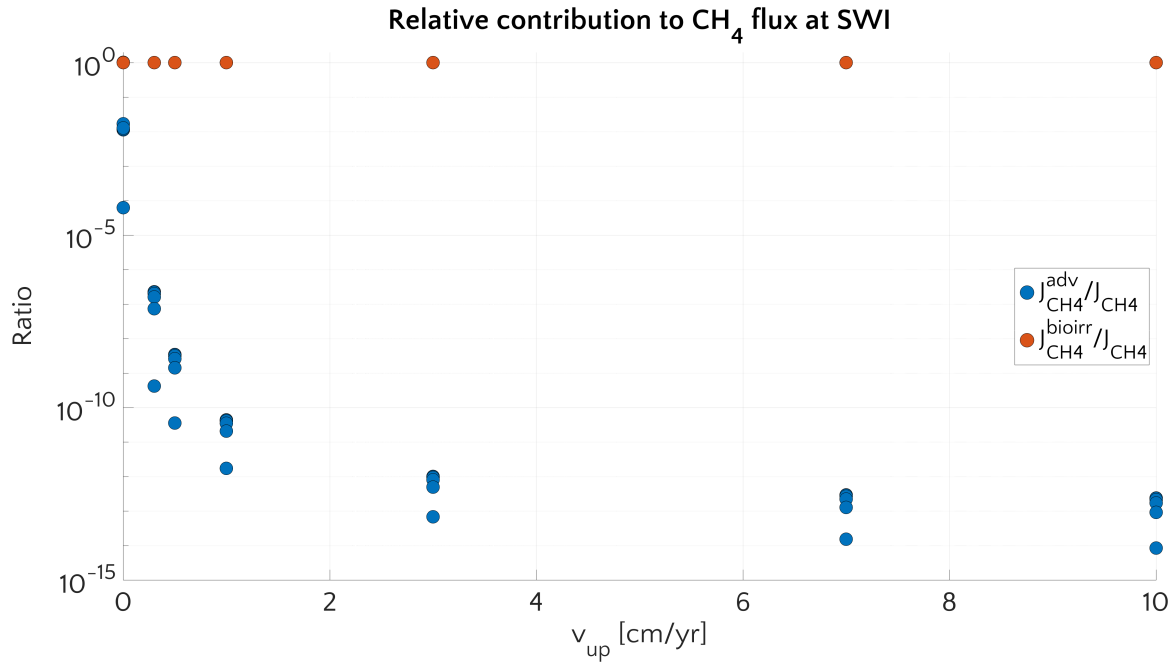

Figure S3. Relative contribution of transport process to the methane flux at the SWI: the advective component (blue) and the bioirrigation component (red). ω is set to the baseline value of 0.123 cm yr^{-1}. For each value of v_{up} and a specific flux component each dot corresponds to a simulation with a different value of bottom CH_4 concentration. Diffusive component of the flux is always $< 10^{-10}$.

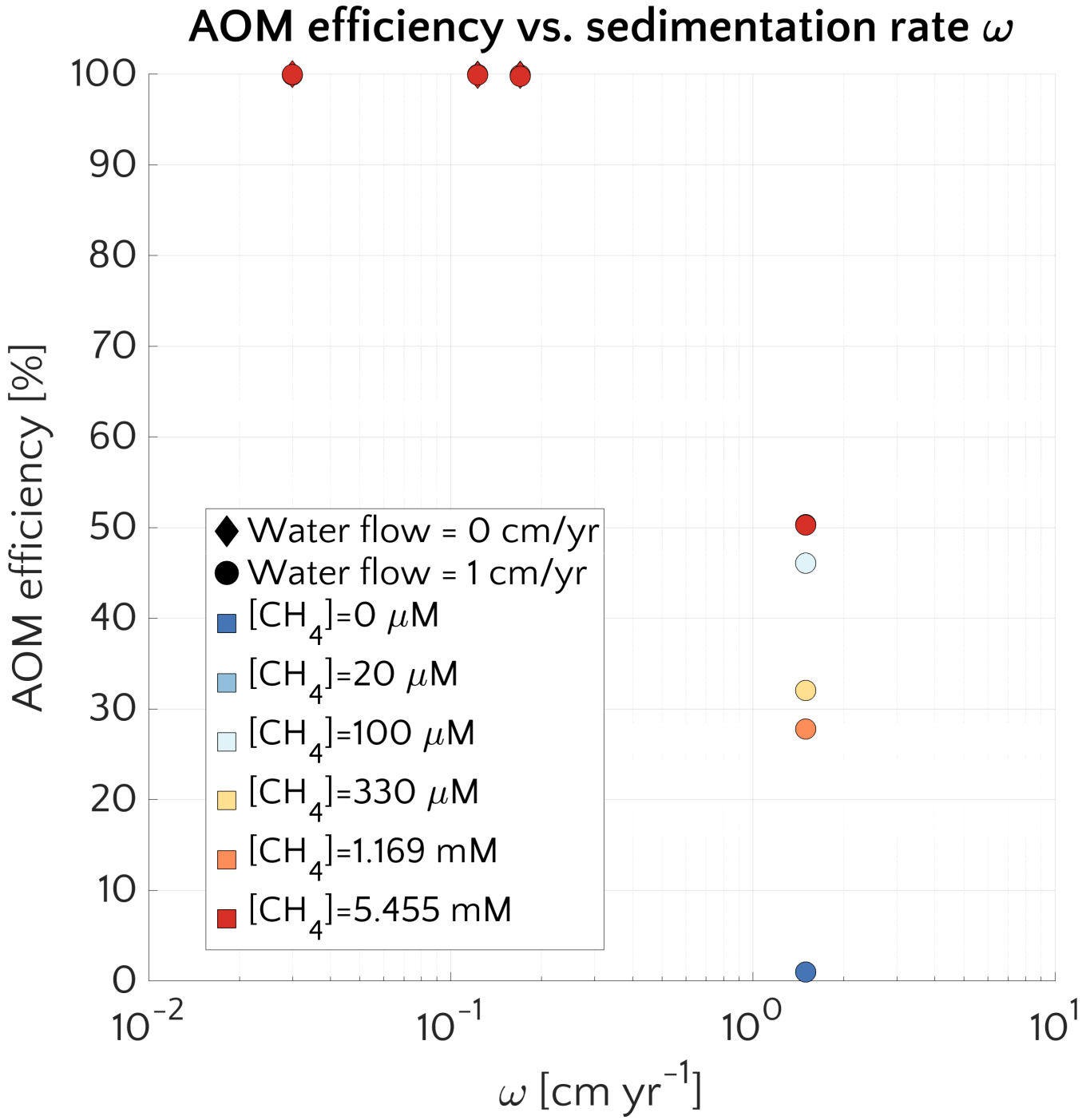

Figure S4. AOM filter efficiency η versus ω for passive cases (diamonds) and active cases (circles).

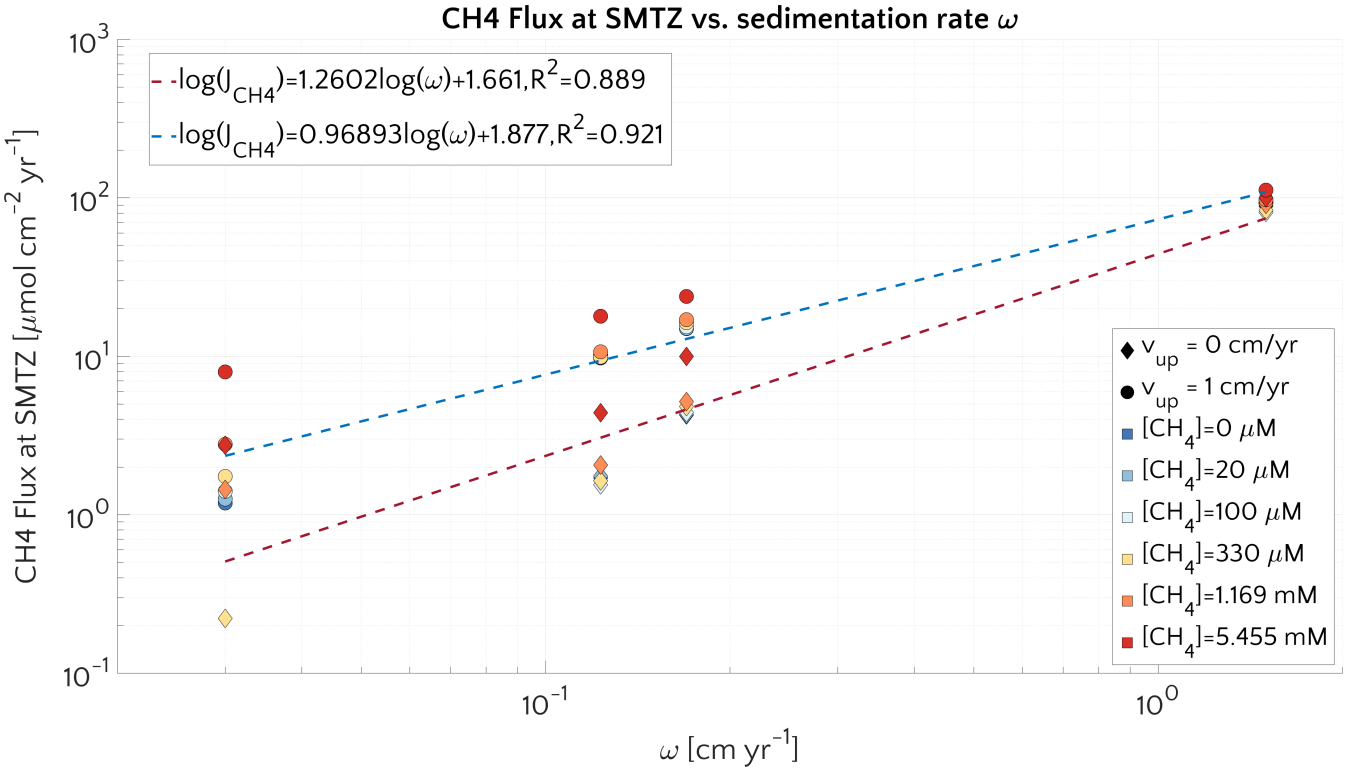

Figure S5. Methane flux at the centre of SMTZ versus ω for passive (diamonds) and active (circle) cases. Log-log fit is reported.

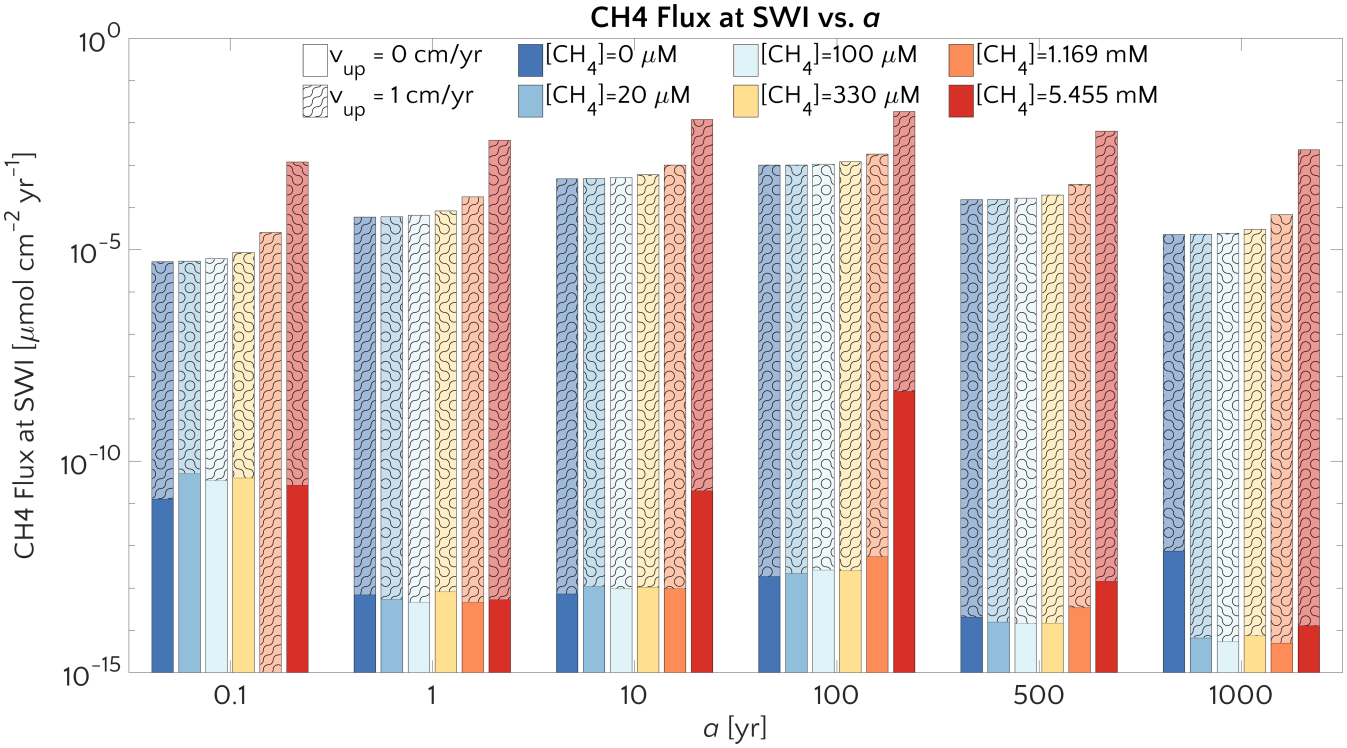

Figure S6. Barplot of the methane flux at the SWI versus a for passive case (plain) and active case (pattern) and the $[CH_4]_-$ reported in the text.

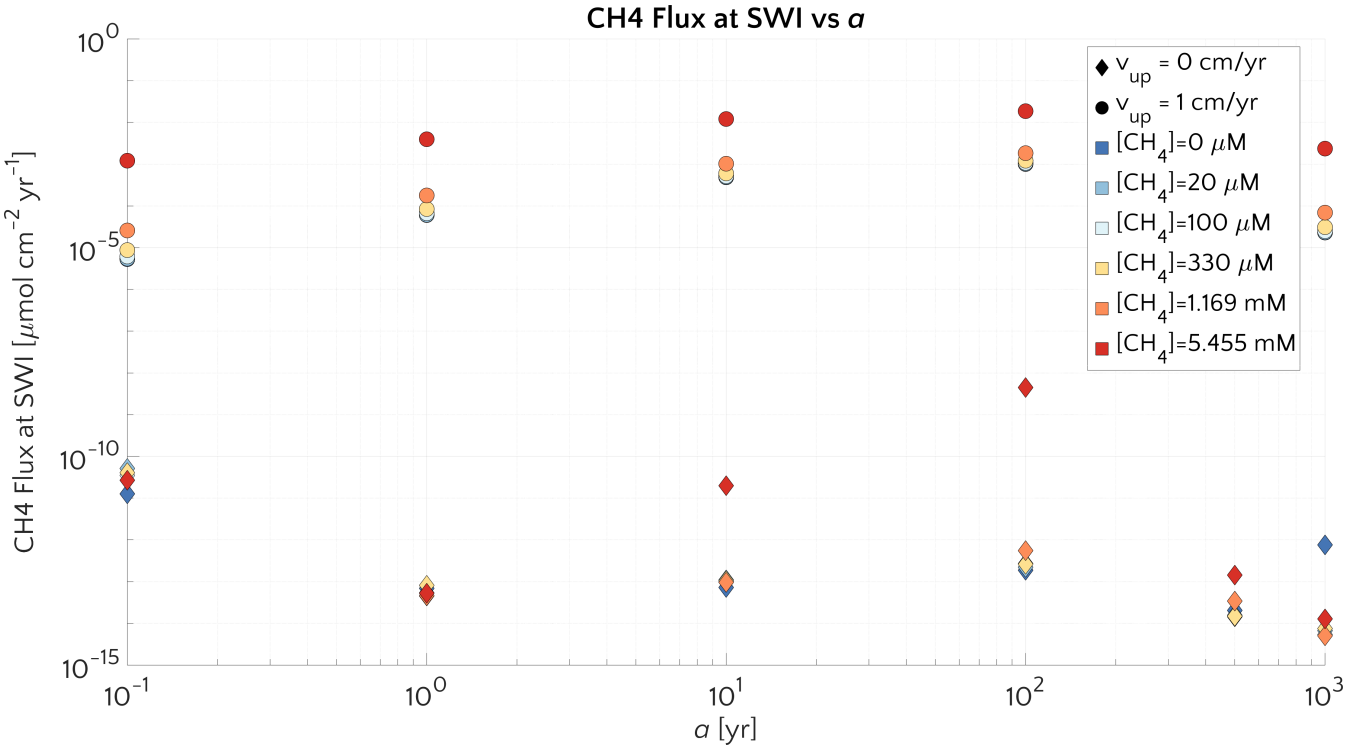

Figure S7. Methane flux at SWI versus a for passive (diamonds) and active (circle) cases.

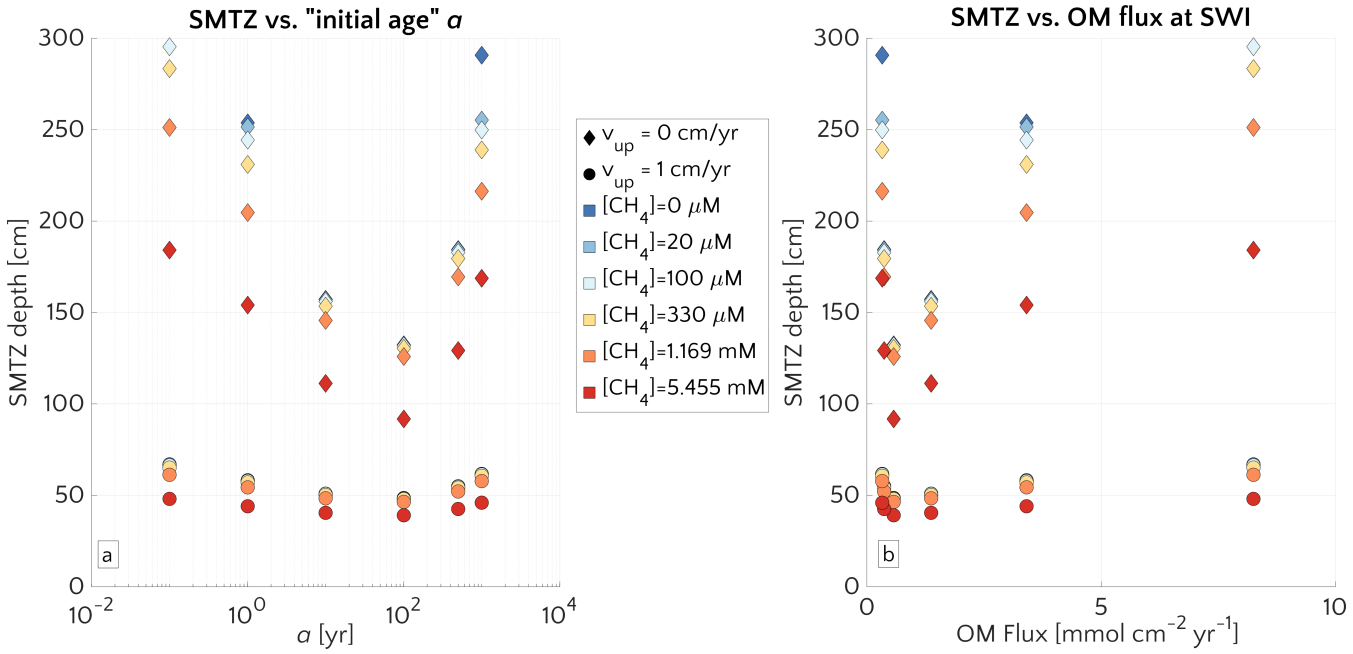

Figure S8. (a) SMTZ depth versus a. Passive (diamonds) and active (circle) cases for different $[\mathrm{CH_4}]_-$. (b) SMTZ depth versus OM flux entering the system at the SWI.

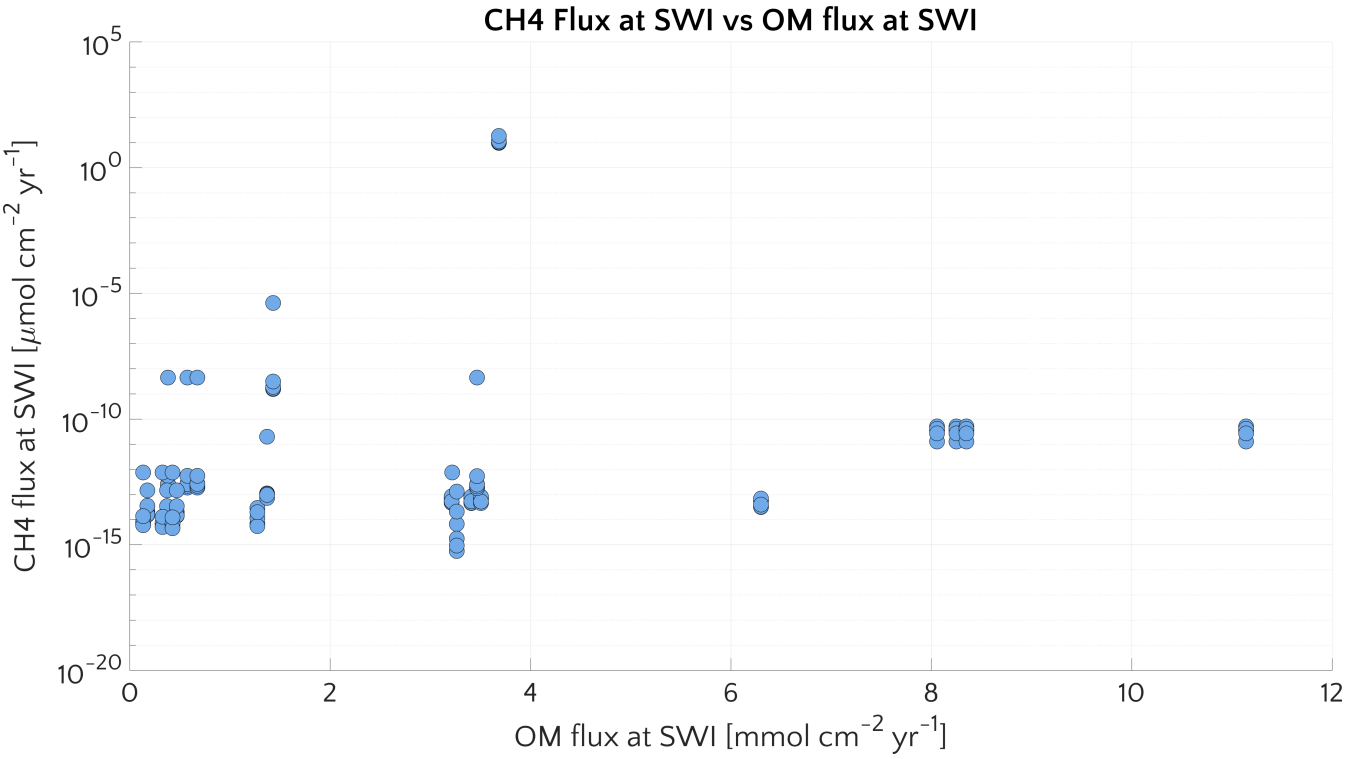

Figure S9. Methane flux at SWI versus OM flux at SWI

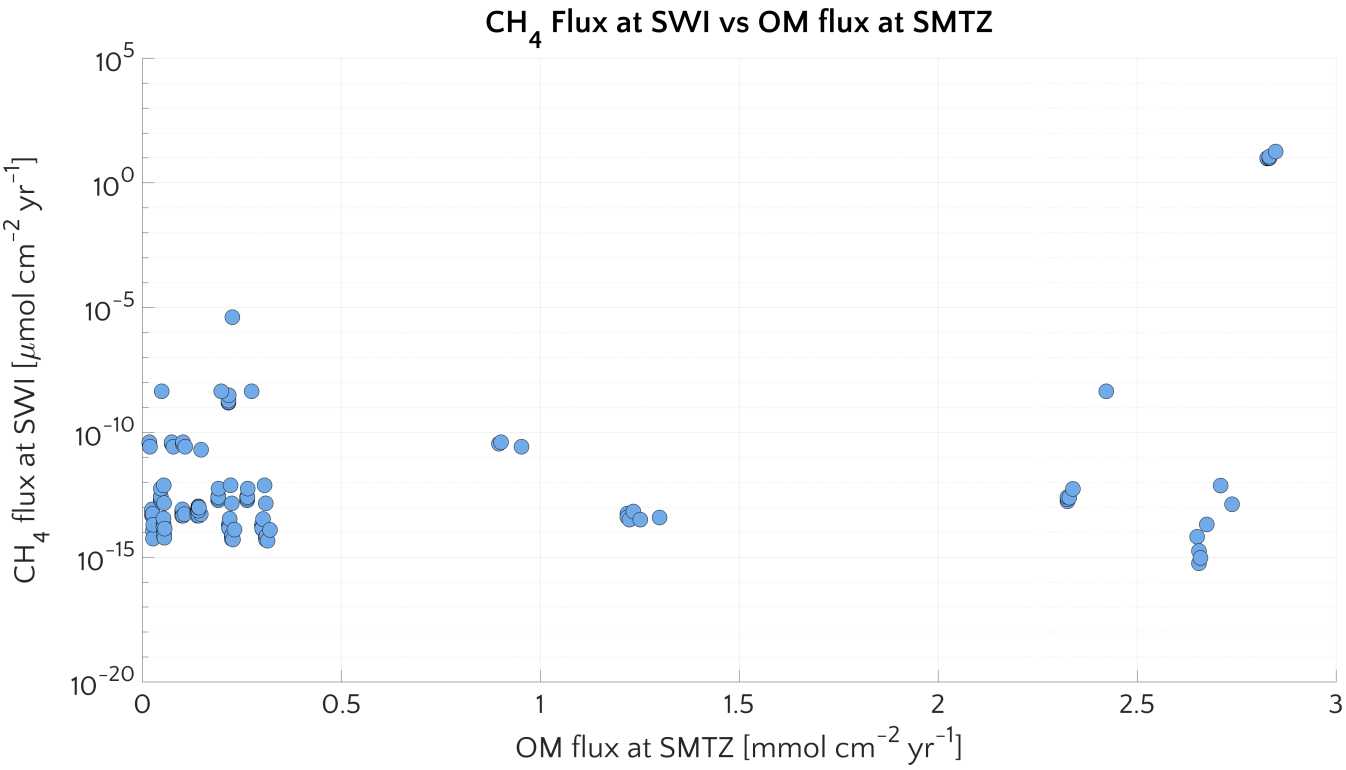

Figure S10. Methane flux at SWI versus OM flux at SMTZ

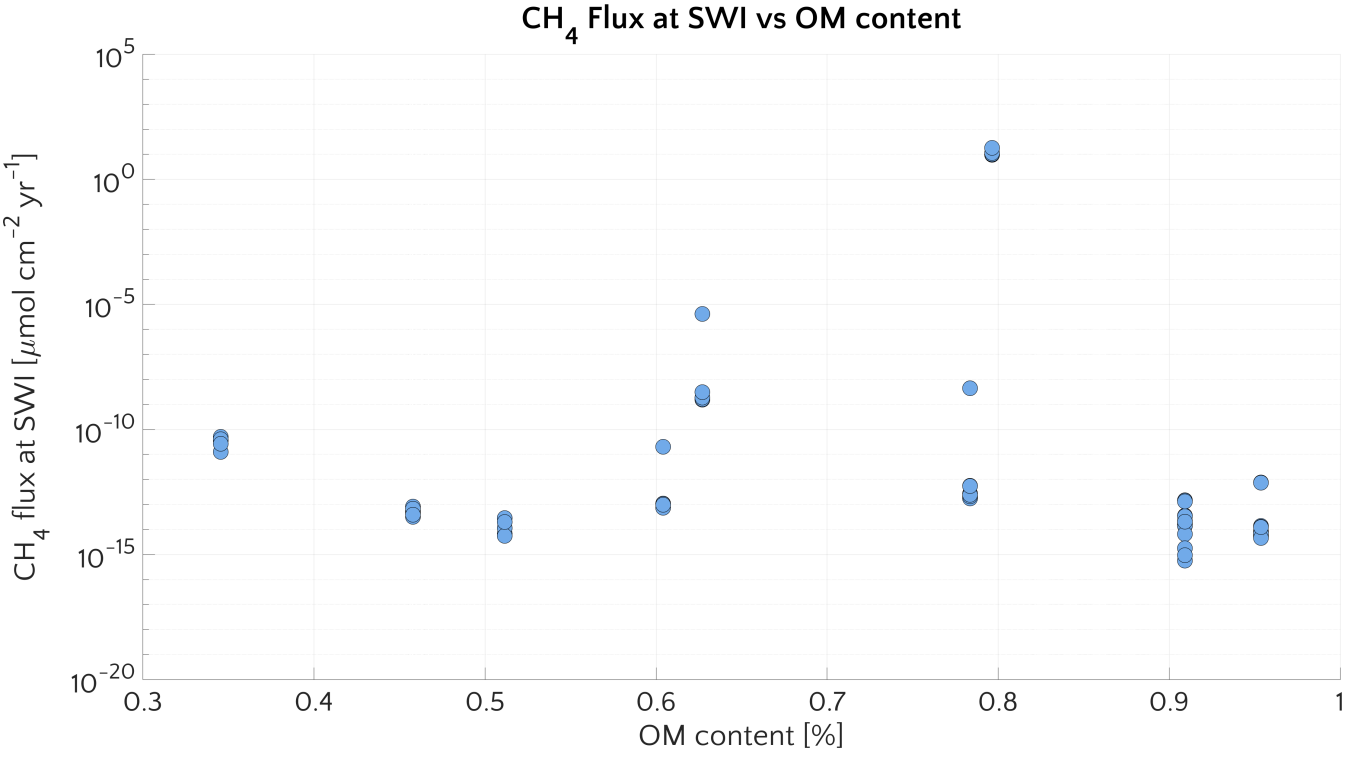

Figure S11. Methane flux at SWI versus OM sediment content

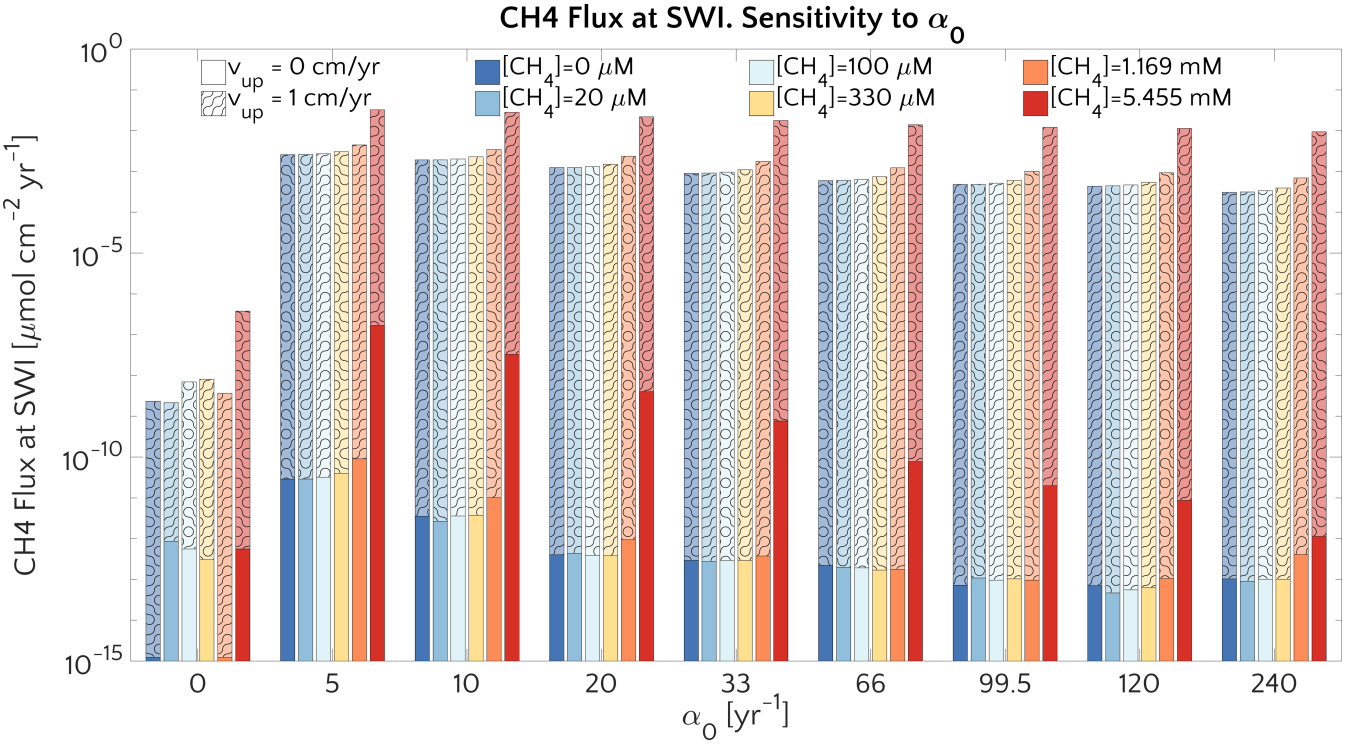

Figure S12. Barplot of the methane flux at the SWI versus α_0 for passive case (plain style) and active case (pattern style) and the $[CH_4]$– analyzed.

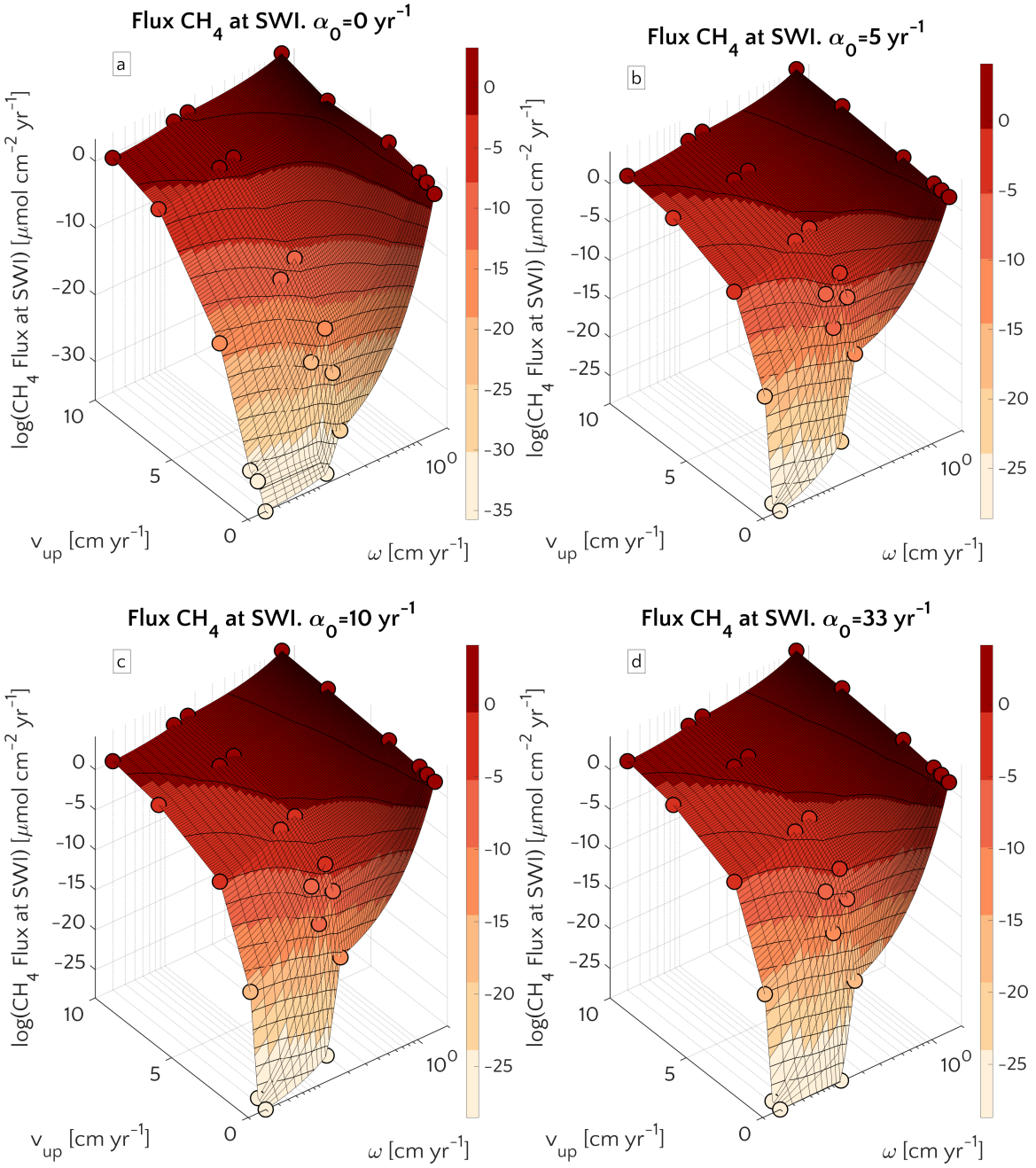

Figure S13. 3D plot of efflux of methane at the SWI as dependent on v_{up} and ω for $\alpha_0 = 0$ yr^{-1} (*a*), $\alpha_0 = 5$ yr^{-1} (*b*), $\alpha_0 = 10$ yr^{-1} (*c*) and $\alpha_0 = 33$ yr^{-1} (*d*). Circles represent simulations outcomes. Results for $\alpha_0 \neq 0$ yr^{-1} are almost the same. The lower boundary condition for methane is $[CH_4]_- = 1.169$ mM.

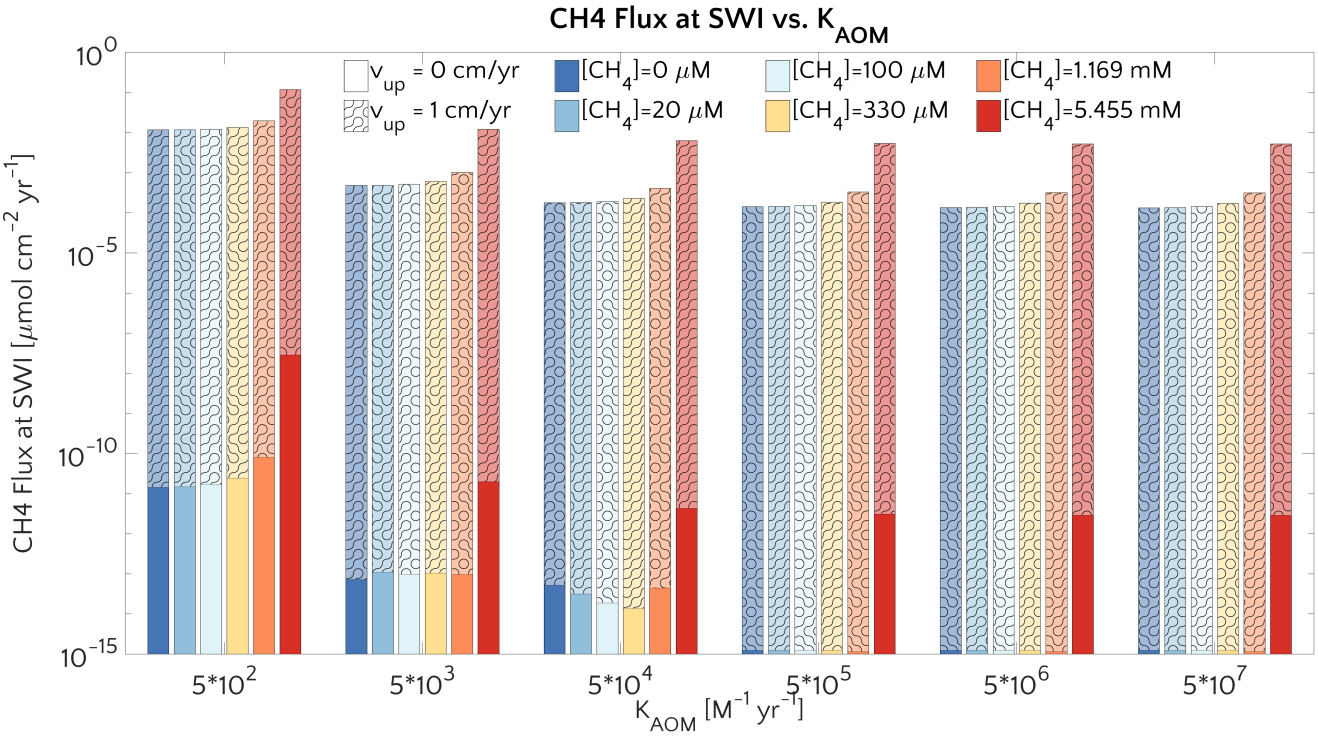

Figure S14. Methane flux at SWI versus AOM reactivity constant k_{AOM}

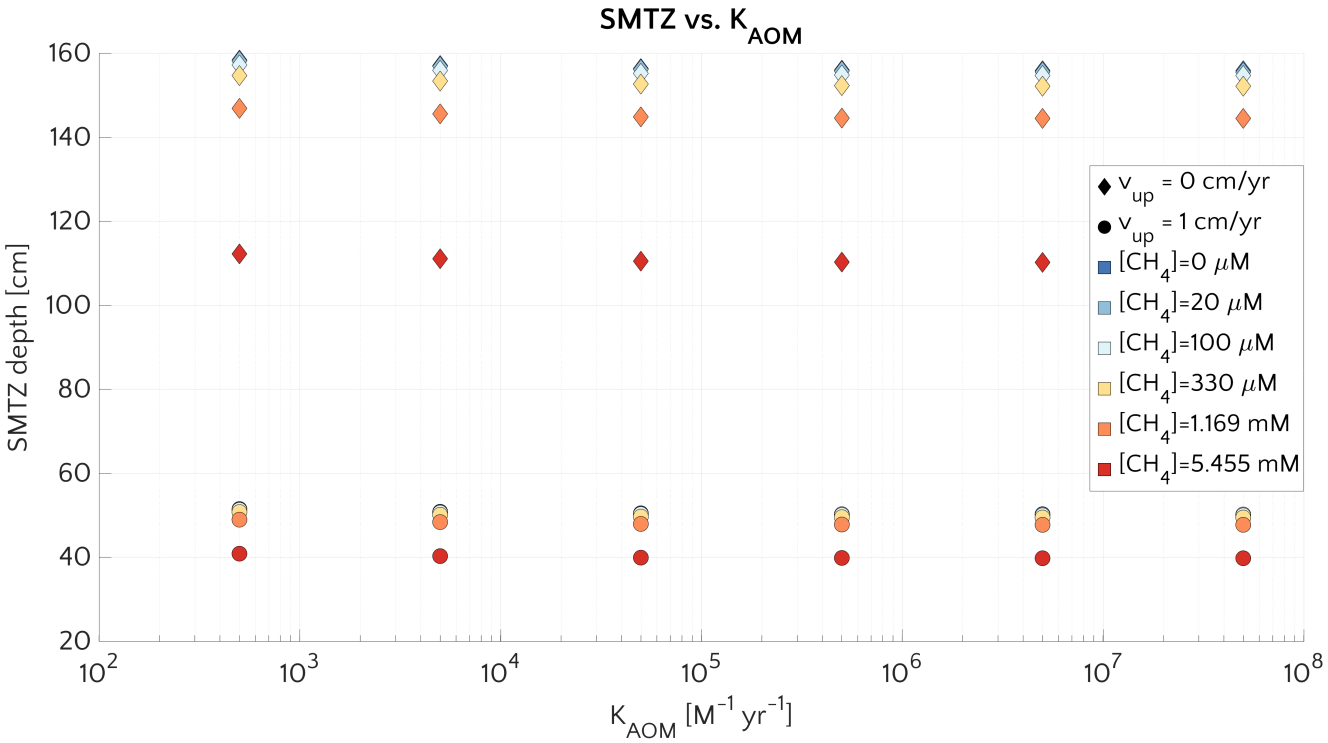

Figure S15. SMTZ depth versus k_{AOM}. Passive (diamonds) and active (circle) cases for different $[\mathrm{CH}_4]_-$.

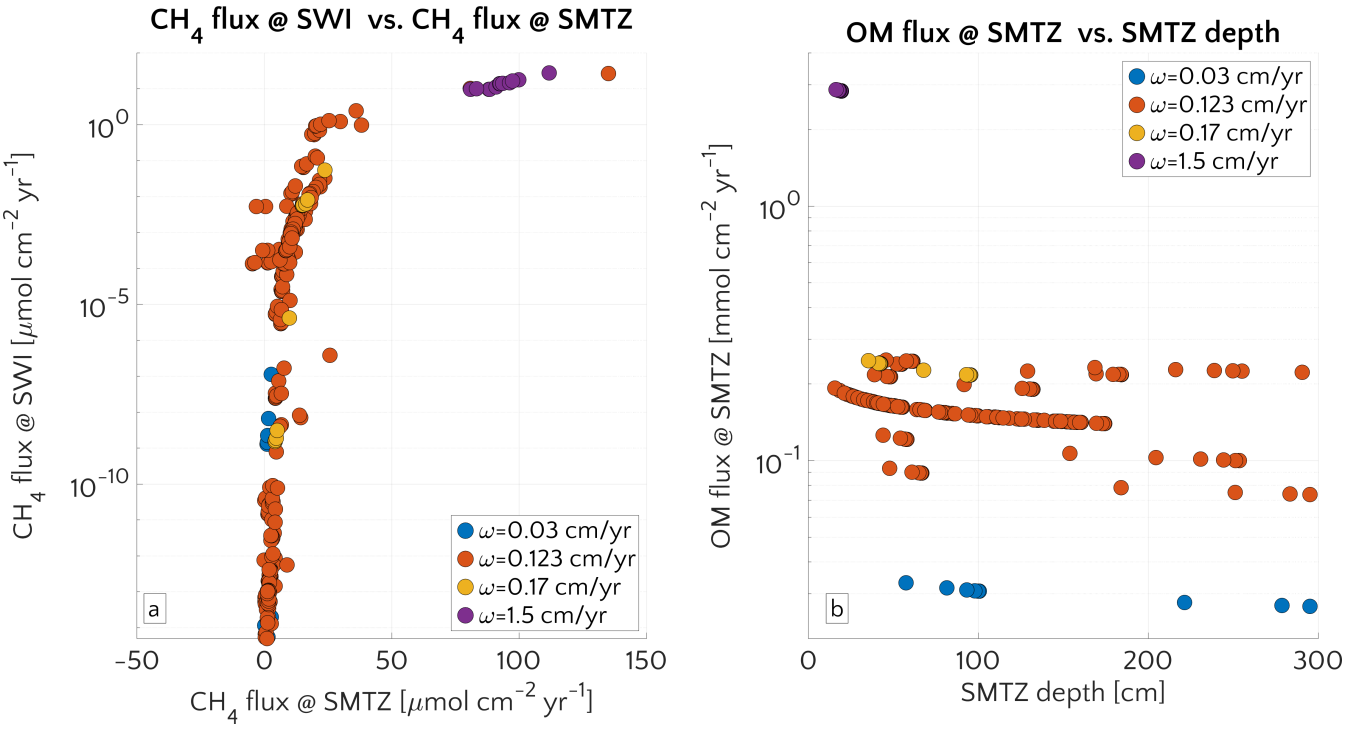

Figure S16. *a.* Flux of methane at SWI versus flux of methane at the SMTZ depth. *b.* OM flux at the SMTZ depth versus SMTZ depth itself. Colours identify simulations with different ω.

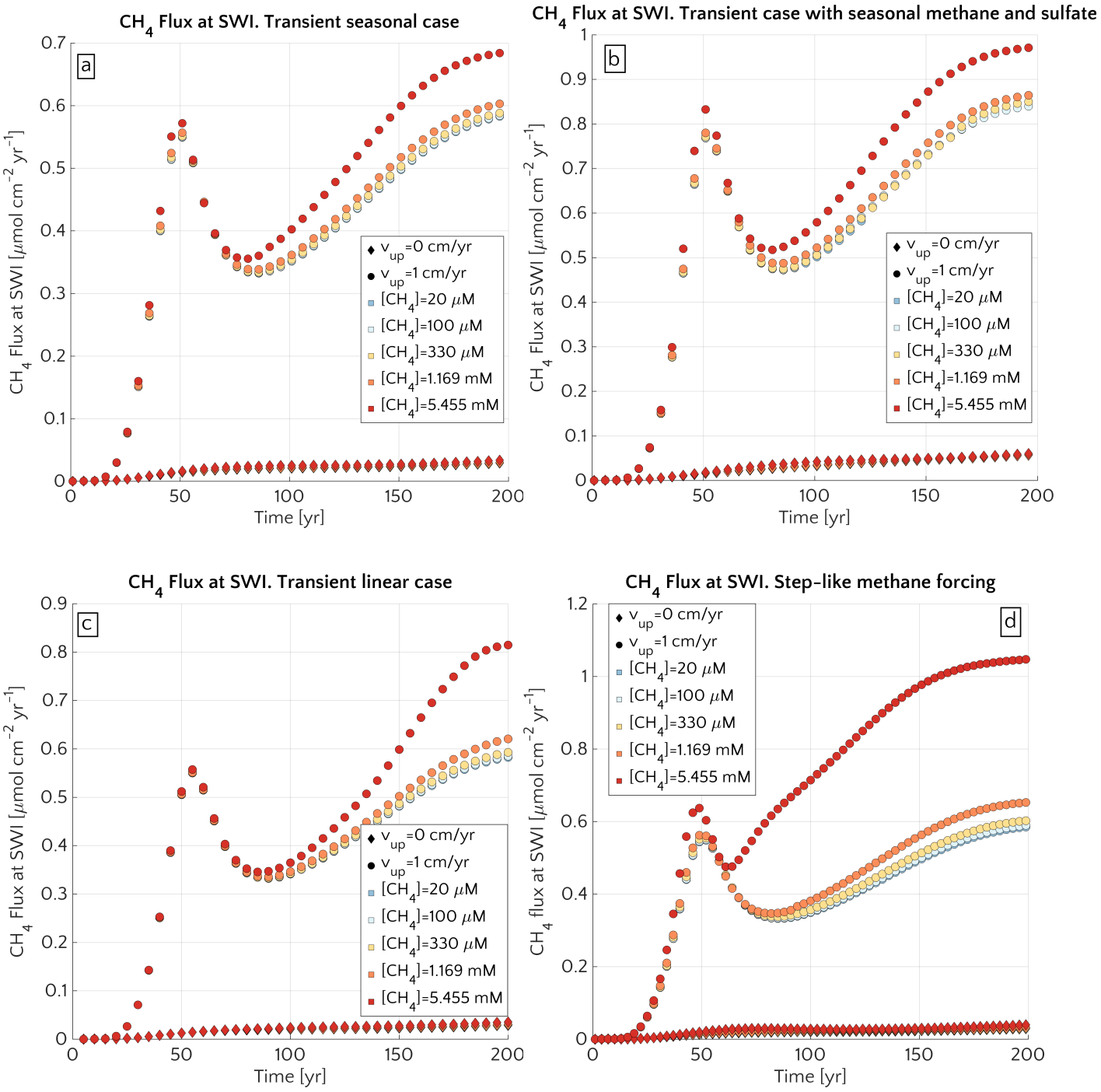

Figure S17. Flux of methane at SWI over time for passive (diamonds) and active (circle) setups and different $[CH_4]_-$. *a.* Seasonal methane forcing from below. *b.* Seasonal methane forcing from below and seasonal sulfate forcing from above. *c.* Linear methane forcing from below. *d.* Step-like methane forcing from below.

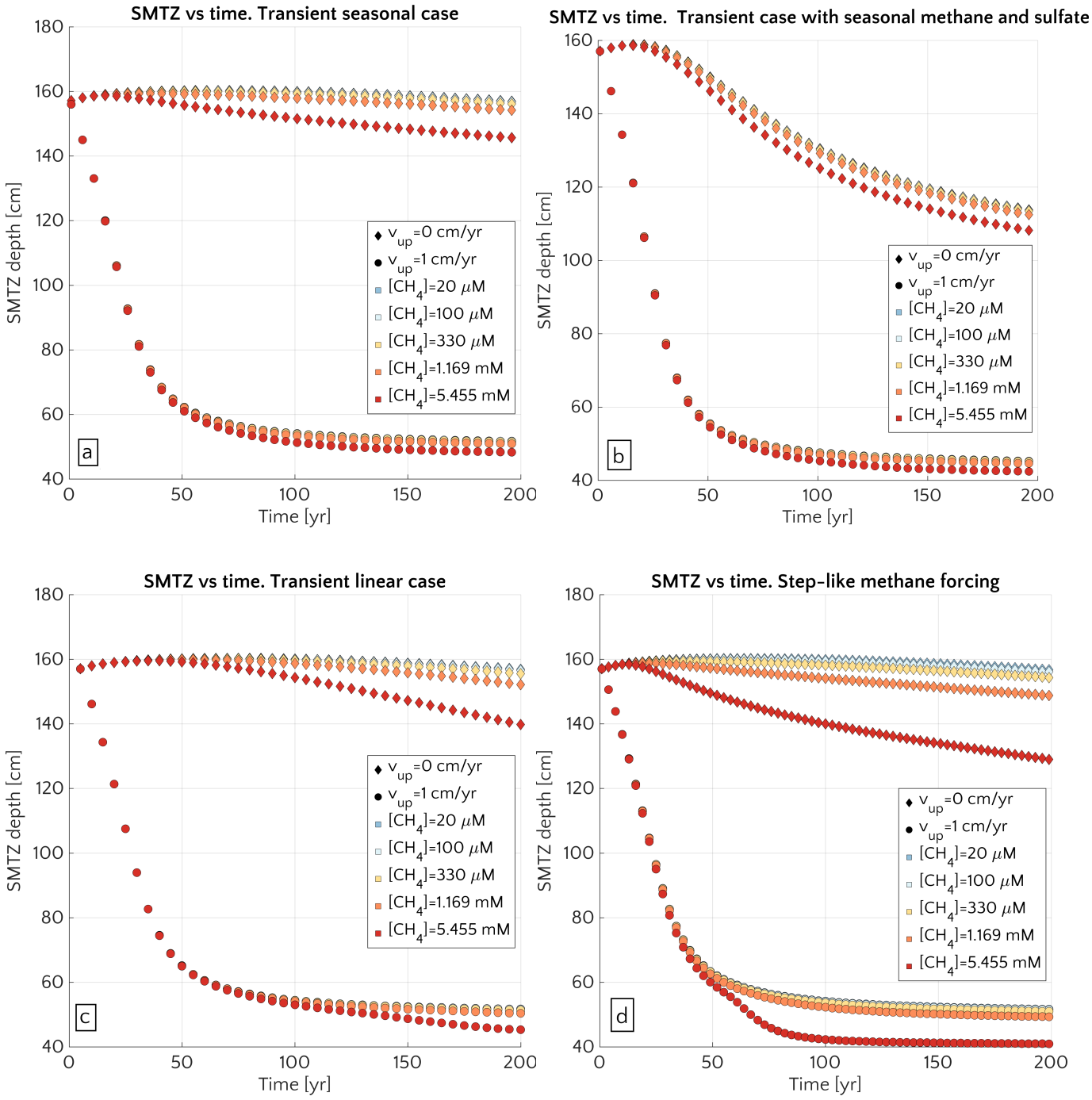

Figure S18. Movement of SMTZ over time for passive (diamonds) and active (circle) setups and different $[CH_4]_-$. *a.* Seasonal methane forcing from below. *b.* Seasonal methane forcing from below and seasonal sulfate forcing from above. *c.* Linear methane forcing from below. *c.* Step-like methane forcing from below.

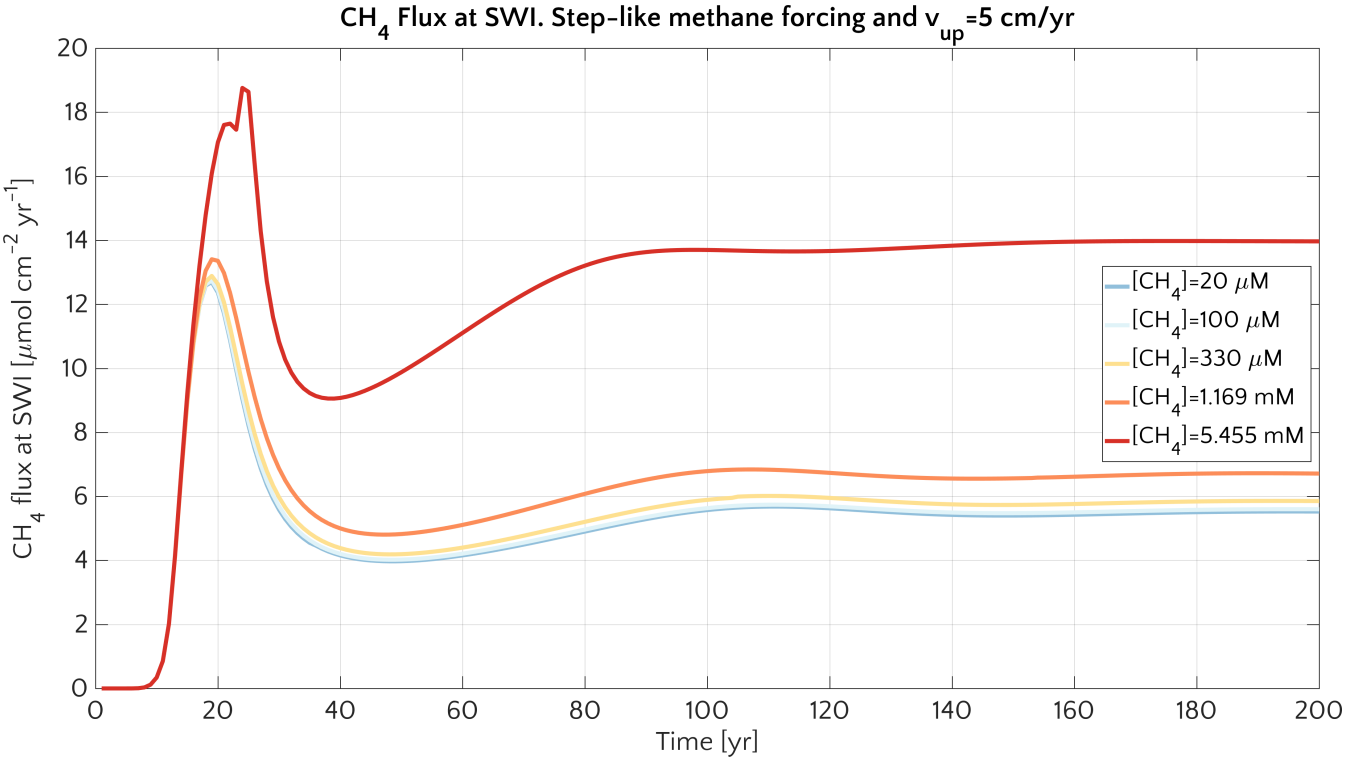

Figure S19. Flux of methane at SWI versus time for scenario 4 (step-like methane increase) and $v_{up} = 5$ cm/yr. Colours identify simulations with different CH_4 bottom concentrations.

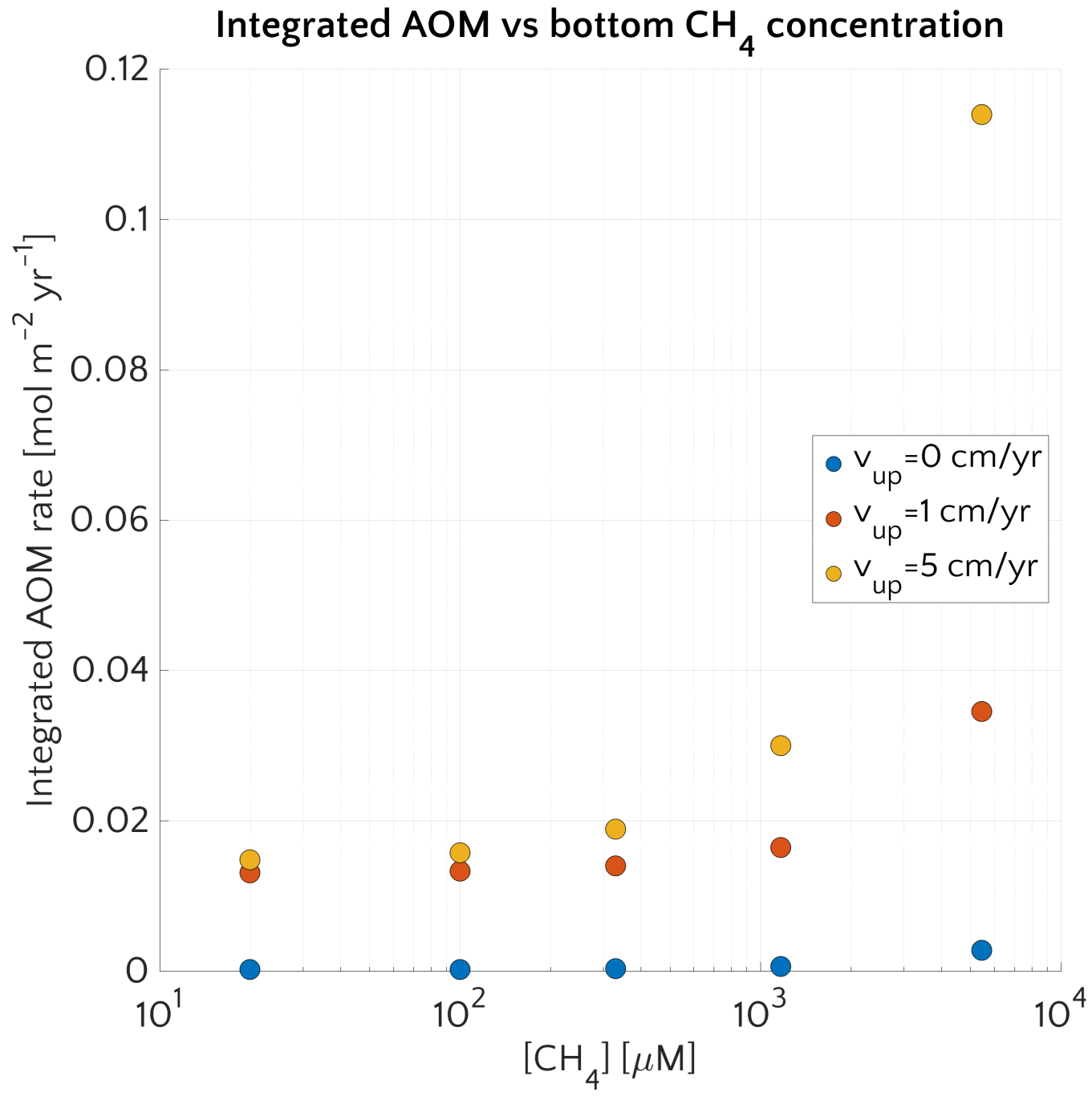

Figure S20. Vertically integrated AOM *vs* the bottom methane concentration $[\mathrm{CH}_4]_-$ for three different v_{up}.

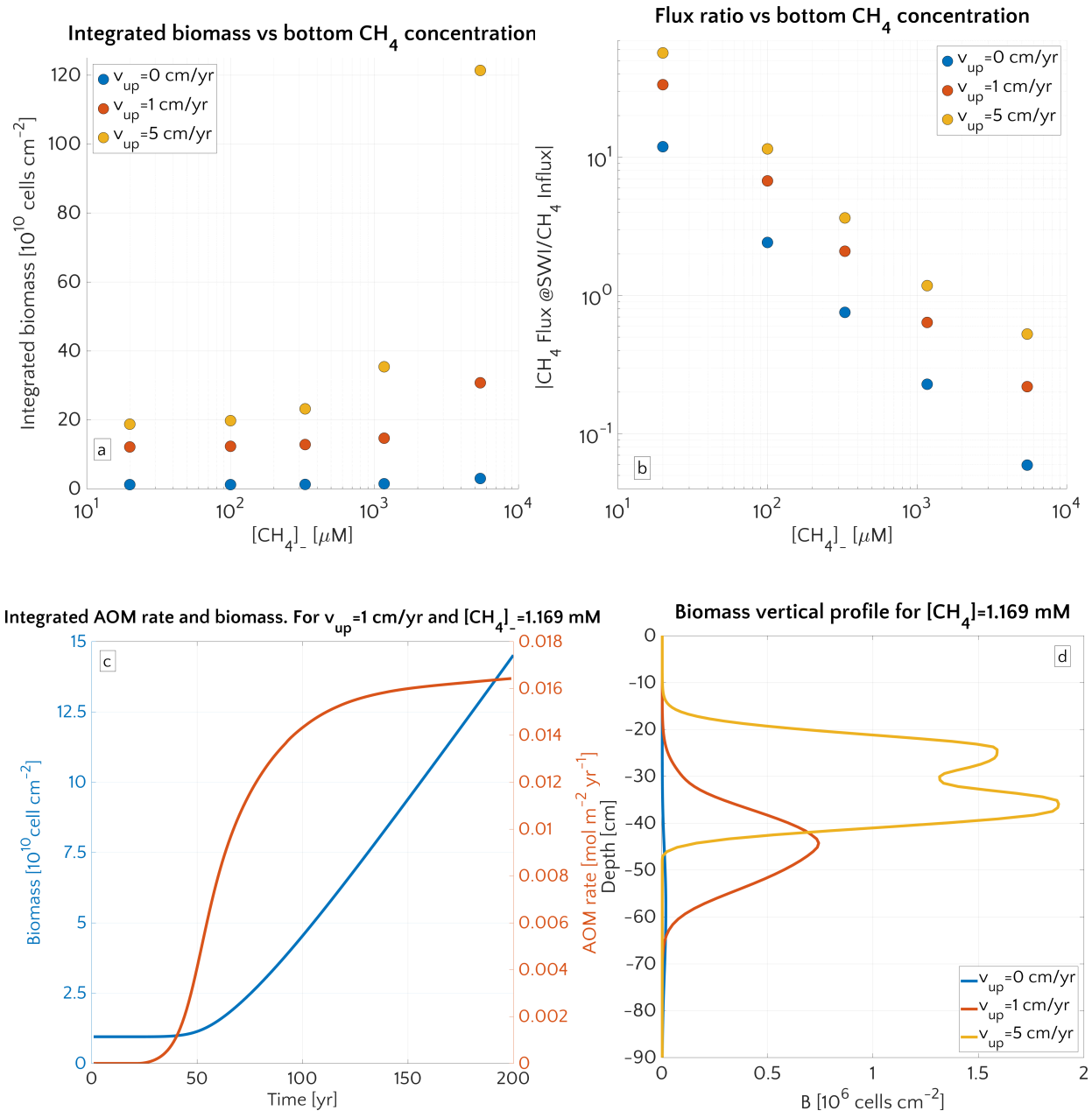

Figure S21. *a.* Vertically integrated biomass after 200 years *vs* the bottom methane concentration $[\mathrm{CH_4}]_-$ for three different v_{up}. *b.* Absolute value of the ratio of the methane flux at the SWI to the advective methane flux at the base of sediment column *vs* the bottom methane concentration $[\mathrm{CH_4}]_-$ for three different v_{up}. *c.* Time evolution of the vertically integrated AOM biomass (blue) and vertically integrated AOM rate (red) for the step-like simulation with $[\mathrm{CH_4}]_- = 1.169$ mM and $v_{up} = 1$ cm/yr. *d.* AOM biomass vertical profile after 200 years for three different v_{up} in case of step-like simulation with $[\mathrm{CH_4}]_- = 1.169$ mM.

References

Aller, R. C. and Blair, N. E.: Early diagenetic remineralization of sedimentary organic C in the Gulf of Papua deltaic complex (Papua New Guinea): net loss of terrestrial C and diagenetic fractionation of C isotopes, Geochimica et Cosmochimica Acta, 68, 1815–1825, 2004.

Arndt, S., Jørgensen, B. B., LaRowe, D. E., Middelburg, J., Pancost, R., and Regnier, P.: Quantifying the degradation of organic matter in marine sediments: a review and synthesis, Earth-science reviews, 123, 53–86, 2013.

Athy, L. F.: Density, porosity, and compaction of sedimentary rocks, AAPG Bulletin, 14, 1–24, 1930.

Bauch, H. A., Mueller-Lupp, T., Taldenkova, E., Spielhagen, R. F., Kassens, H., Grootes, P. M., Thiede, J., Heinemeier, J., and Petryashov, V.: Chronology of the Holocene transgression at the North Siberian margin, Global and Planetary Change, 31, 125–139, 2001.

Berg, P.: Dynamic Modeling of Early Diagenesis and Nutrient Cycling. A Case Study in an Artic Marine Sediment, American Journal of Science, 303, 905–955, 2003.

Berner, R. A.: Early diagenesis: a theoretical approach, 1, Princeton University Press, 1980.

Boudreau, B. P.: Diagenetic models and their implementation, vol. 505, Springer Berlin, 1997.

Boudreau, B. P. and Ruddick, B. R.: On a reactive continuum representation of organic matter diagenesis, American Journal of Science, 291, 507–538, 1991.

Brüchert, V.: Unpublished raw data, 2020.

Brüchert, V., Bröder, L., Sawicka, J. E., Tesi, T., Joye, S. P., Sun, X., Semiletov, I. P., and Samarkin, V. A.: Carbon mineralization in Laptev and East Siberian sea shelf and slope sediment, Biogeosciences, 15, 471–490, 2018.

Claypool, G. E. and Kaplan, I.: The origin and distribution of methane in marine sediments, in: Natural gases in marine sediments, pp. 99–139, Springer, 1974.

Dale, A. W., Regnier, P., and Van Cappellen, P.: Bioenergetic controls on anaerobic oxidation of methane (AOM) in coastal marine sediments: a theoretical analysis, American Journal of Science, 306, 246–294, 2006.

Dale, A. W., Aguilera, D., Regnier, P., Fossing, H., Knab, N., and Jørgensen, B. B.: Seasonal dynamics of the depth and rate of anaerobic oxidation of methane in Aarhus Bay (Denmark) sediments, Journal of Marine Research, 66, 127–155, 2008a.

Dale, A. W., Van Cappellen, P., Aguilera, D., and Regnier, P.: Methane efflux from marine sediments in passive and active margins: Estimations from bioenergetic reaction–transport simulations, Earth and Planetary Science Letters, 265, 329–344, 2008b.

Dale, A. W., Meyers, S. R., Aguilera, D. R., Arndt, S., and Wallmann, K.: Controls on organic carbon and molybdenum accumulation in Cretaceous marine sediments from the Cenomanian–Turonian interval including Oceanic Anoxic Event 2, Chemical Geology, 324-325, 28–45, 2012.

Dale, A. W., Nickelsen, L., Scholz, F., Hensen, C., Oschlies, A., and Wallmann, K.: A revised global estimate of dissolved iron fluxes from marine sediments, Global Biogeochemical Cycles, 29, 691–707, https://doi.org/10.1002/2014gb005017, https://doi.org/10.1002%2F2014gb005017, 2015.

Froelich, P., Klinkhammer, G., Bender, M. L., Luedtke, N., Heath, G. R., Cullen, D., Dauphin, P., Hammond, D., Hartman, B., and Maynard, V.: Early oxidation of organic matter in pelagic sediments of the eastern equatorial Atlantic: suboxic diagenesis, Geochimica et cosmochimica acta, 43, 1075–1090, 1979.

Garcia, H. E., Boyer, T. P., Locarnini, R. A., Antonov, J. I., Mishonov, A. V., Baranova, O. K., Zweng, M. M., Reagan, J. R., Johnson, D. R., and Levitus, S.: World Ocean Atlas 2009, Volume 3: Dissolved Oxygen, Apparent Oxygen Utilization, and Oxygen Saturation, 2010a.

Garcia, H. E., Locarnini, R. A., Boyer, T. P., Antonov, J. I., Baranova, O. K., Zweng, M. M., Reagan, J. R., Johnson, D. R., Mishonov, A. V., and Levitus, S.: World Ocean Atlas 2009, Volume 4: Nutrients (phosphate, nitrate, silicate), 2010b.

Glasby, G. P.: Manganese: predominant role of nodules and crusts, in: Marine geochemistry, pp. 371–427, Springer, 2006.

Han, P.: Characteristics and sedimentation rates at the shallow Laptev Sea, Master's thesis, University of Bremen, 2014.

LaRowe, D. E., Burwicz, E., Arndt, S., Dale, A. W., and Amend, J. P.: Temperature and volume of global marine sediments, Geology, 45, 275–278, 2017.

Meile, C. and Van Cappellen, P.: Particle age distributions and O2 exposure times: Timescales in bioturbated sediments, Global biogeochemical cycles, 19, 2005.

Middelburg, J. J., Soetaert, K., and Herman, P. M.: Empirical relationships for use in global diagenetic models, Deep Sea Research Part I: Oceanographic Research Papers, 44, 327–344, 1997.

Millero, F. J.: Thermodynamics of the carbon dioxide system in the oceans, Geochimica et Cosmochimica Acta, 59, 661–677, https://doi.org/10.1016/0016-7037(94)00354-o, https://doi.org/10.1016%2F0016-7037%2894%2900354-o, 1995.

Mucci, A.: The solubility of calcite and aragonite in seawater at various salinities, temperatures, and one atmosphere total pressure, American Journal of Science, 283, 780–799, https://doi.org/10.2475/ajs.283.7.780, https://doi.org/10.2475%2Fajs.283.7.780, 1983.

Pauss, A., Andre, G., Perrier, M., and Guiot, S. R.: Liquid-to-gas mass transfer in anaerobic processes: inevitable transfer limitations of methane and hydrogen in the biomethanation process, Appl. Environ. Microbiol., 56, 1636–1644, 1990.

Regnier, P., Dale, A. W., Arndt, S., LaRowe, D., Mogollón, J., and Van Cappellen, P.: Quantitative analysis of anaerobic oxidation of methane (AOM) in marine sediments: a modeling perspective, Earth-Science Reviews, 106, 105–130, 2011.

Sales de Freitas, F.: Deciphering the relationships between reactivity and sources of organic matter in marine sediments: a coupled large-scale model and lipid biomarker analysis, Ph.D. thesis, School on Earth Sciences, University of Bristol, 2018.

Stein, R. and Fahl, K.: Holocene accumulation of organic carbon at the Laptev Sea continental margin (Arctic Ocean): sources, pathways, and sinks, Geo-Marine Letters, 20, 27–36, https://doi.org/10.1007/s003670000028, https://doi.org/10.1007%2Fs003670000028, 2000.

Stein, R., Boucsein, B., Fahl, K., de Oteyza, T. G., Knies, J., and Niessen, F.: Accumulation of particulate organic carbon at the Eurasian continental margin during late Quaternary times: controlling mechanisms and paleoenvironmental significance, Global and Planetary Change, 31, 87–104, 2001.

Strobl, C., Schulz, V., Vogler, S., Baumann, S., Kassens, H., Kubik, P., Suter, M., and Mangini, A.: Determination of depositional beryllium-10 fluxes in the area of the Laptev Sea and beryllium-10 concentrations in water samples of high northern latitudes, in: Land-Ocean Systems in the Siberian Arctic, pp. 515–532, Springer, 1998.

Stumm, W. and Morgan, J. J.: Aquatic Chemistry: Chemical Equilibria and Rates in Natural Waters {Environmental Science and Technology}, Wiley, 1996.

Thullner, M., Dale, A. W., and Regnier, P.: Global-scale quantification of mineralization pathways in marine sediments: A reaction-transport modeling approach, Geochemistry, geophysics, geosystems, 10, 2009.

Van Cappellen, P. and Wang, Y.: Cycling of iron and manganese in surface sediments; a general theory for the coupled transport and reaction of carbon, oxygen, nitrogen, sulfur, iron, and manganese, American Journal of Science, 296, 197–243, 1996.

Wallmann, K., Aloisi, G., Haeckel, M., Obzhirov, A., Pavlova, G., and Tishchenko, P.: Kinetics of organic matter degradation, microbial methane generation, and gas hydrate formation in anoxic marine sediments, Geochimica et Cosmochimica Acta, 70, 3905–3927, 2006.